Assessing dependency of part properties on the printing location in laser-powder bed fusion metal additive manufacturing

Andre Mussatto[1, 2, 3, a], Robert Groarke[1, 2, 3], Rajani K. Vijayaraghavan[2, 3, 4], Cian Hughes[1, 2, 3], Muhannad Ahmed Obeidi[1, 2, 3], Merve Nur Doğu[1, 2, 3], Mustafa Alp Yalçın[5], Patrick J. McNally[2, 3, 4], Yan Delaure[1, 2, 3], Dermot Brabazon[1, 2, 3]

[1] School of Mechanical and Manufacturing Engineering, Dublin City University, Glasnevin, Ireland

[2] I-Form Advanced Manufacturing Research Centre, Dublin City University, Glasnevin, Ireland

[3] Advanced Processing Technology Research Centre, Dublin City University, Glasnevin, Ireland

[4] School of Electronic Engineering, Dublin City University, Glasnevin, Ireland

[5] Metal Forming Center of Excellence, Atılım University, Ankara, Turkey

[a] Corresponding author: andre.mussatto2@mail.dcu.ie

Abstract

Despite the accelerated growth of laser-powder bed fusion in recent years, there are still major obstacles to be overcome before the technology enjoys truly widespread adoption. These include inconsistent part quality and repeatability issues linked to variability in the properties of printed parts. Commonly, the print location across the build platform is overlooked and assumed to have little or no effect on the overall part properties. There is a lack of previous systematic studies and a lack of knowledge of the influences of the location parameter on the final part properties. Therefore, to address the existing problem, the current study completely isolated the location parameter to accurately assess any effect of this variable on the microstructure and mechanical properties of laser-powder bed fusion manufactured parts. The results revealed the importance of the build location and showed that there is correlation between the location parameter and part properties as qualitative and quantitative properties of printed parts varied between the selected extremity locations. The findings highlight the importance of considering the location of the part being printed on the build platform and how the location may need to be fixed for multiple builds in order to achieve acceptable repeatability.

Keywords: powder bed fusion; part location; repeatability; stainless steel; corrosion

1. Introduction

In recent years, laser-powder bed fusion (L-PBF) has been gaining increasing industrial attention for the production of functional components as it offers a step change in the possibilities of design and manufacturing [1]. L-PBF enables the manufacturing of components exhibiting complex features, innovative shapes and lightweight structures that are difficult or even impossible to manufacture with conventional techniques [2,3]. In this context, ensuring the quality, repeatability and reproducibility of L-PBF manufactured components is fundamental to meet the stringent requirements and certification constraints imposed by leading industries such as aerospace, automotive and medical [4]. Unfortunately, the lack of process robustness, stability and repeatability has been identified as a major barrier for the industrial breakthrough of L-PBF [5,6]. In fact, despite significant technological advances, the defect rates are still too high with respect to conventional techniques.

Achieving high levels of quality, repeatability and reproducibility of L-PBF components is extremely challenging due to a multitude of factors, such as the high number of processing variables and the physics of the underlying phenomena and transformations that take place during component manufacturing [7]. To overcome some of these challenges substantial work has been carried out on key processing parameters (laser, scanning, recoating and build environment parameters) and powder bed properties. Also, considerable emphasis has recently been placed on process monitoring and feedback control strategies [8]. However, L-PBF has over 100 processing parameters, some of which, along with their interactions have gained little or no attention yet [9].

The location, a processing parameter of L-PBF, refers to the printing location of a part on the build platform [10]. It can cause intra-build variations that occur within one build space and potentially within one part. Recently, the location parameter has been a matter of research as it was suspected to be a contributor to variation in the final microstructure characteristics and mechanical performance of printed parts [11]. It was reported that the location

can influence the final surface roughness [12]. In fact, a smoother finishing was achieved in parts located in the area close to the gas inlet and towards the build platform back location [13]. Nevertheless, thin parts having high aspect ratios are more sensitive to critical locations, thus requiring a more careful consideration [14]. It was also reported that the generation of oxidation spots and lack of fusion defects can also arise from the location parameter [15]. In this respect, the presence of oxidation spots was then attributed to the inert gas flow turbulences and so inefficiencies in preventing oxidation due to oxygen exposure. Similarly, the lack of fusion defects was related to laser attenuations due to plumes of fine particles formed from the evaporated material, to which the inert gas flow failed to ensure the laser beam quality and stability of the melting process [15,16]. Laser-spattered powder particles are detrimental for the final properties of building parts. It was reported that parts located along the inert gas flow or nearby the gas outlet are more affected by spatter [17]. Inert gas flow is also identified as one significant factor that induces microporosity during the L-PBF process and this was assumed to be due to non-uniform distribution of gas flow across the powder bed [18]. The location was also reported to have an effect on the tensile properties of parts [19,20]. Fracture critical properties are affected by numerous factors such as defect density and microstructure variation. In L-PBF, lack of fusion, cracks and porosities typically progress together with the build direction [21]. Generally assumed to be influenced by local inhomogeneities of thermal fields within the process, part density was reported to be dependent also on the location [22]. Elliptical distortions (intensity distribution and shape) of the laser spot occur when scanning parts located near the edge of the build platform and this is due to high scanner deflection angles. Such a beam profile distortion can cause lack of fusion and produce different defects, including poor dimensional accuracies and porosity depending on the building location [23,24]. The location also affects the fatigue behavior of parts [25]. Higher fatigue life was reported on those parts printed near the front of the build platform. The reduction of fine particles and agglomerates improved powder flowability and this was found to reduce location dependency of the fatigue behavior [25]. It is also well documented that powder bed characteristics (segregation and density) varies substantially throughout the build area [26–28]. Additionally, it was reported that variation in terms of build location is also material-dependent. Therefore, some materials may be more or less sensitive to the location in which they are printed on the build platform [29].

Despite the work noted above, much remains to be systematically investigated. To address this problem, the current study isolated the location parameter to accurately assess any effect of this variable on the microstructure and mechanical properties of L-PBF manufactured parts. The outcomes of this investigation are presented and discussed in this article. However, it was not the objective of this study to critically judge any variations promoted by the location parameter for specific applications as these are dictated depending on the related industry sector requirements.

2. Experimental

2.1 Material and Sample Preparation

In this study, vacuum inert gas atomised micron size (35-50 μm) stainless steel AISI 316L powder supplied by Mimete S.r.l. was used as the feedstock material. Samples were printed with an Aconity Mini (Aconity GmbH, Germany) equipped with an ytterbium fibre laser from IPG, model YLR-200-WC-Y11, 2011 series. The laser beam spot diameter was tested and calibrated within the recommended time as instructed by the printer's manufacturer. Based on the printer's manufacturer, the laser beam intensity at the outer areas of the build platform becomes lower, but in comparison to the central area this difference in spot size and related intensity is so small that this effect can be neglected. The shape of the Gaussian laser beam was ensured by the manufacturer to be circular at the central area of the build platform. However, at high scanner deflection angles such as those required to scan the outer areas of the build platform, distortions to the laser beam cross-section could be introduced. All prints were performed in an argon atmosphere using a volume flow rate of 3 l/min, which kept the oxygen level below 100 ppm. This fresh flow of argon entered the processing chamber through inlets located at the bottom of the build cylinder, bottom of the powder reservoir and middle of the processing chamber, while, the argon filtration and re-circulation unit provided a gas volume flow rate of 200 l/min and a gas velocity of 63 mm/s across the build platform. The argon pressure inside the processing chamber was automatically regulated to 50 mbar above the ambient pressure. To completely isolate the location parameter, all the samples were printed using the same conditions. The laser power, scanning speed, layer thickness, laser spot diameter, hatch distance and hatch translation per layer were set as 150 W, 800 mm/s, 50 μm, 50 μm, 50 μm and 25 μm, respectively. To better assess the effect of location, cubes (5x5x5 mm^3) and cuboids (60x8x8 mm^3) were strategically printed at critical locations on the build platform. These locations are at front, back, argon inlet and argon outlet as shown in Figure 1. The powder recoating starts at front and ends at back. Argon flows across the build platform (140 mm diameter)

from the inlet to the outlet diffusor. The build direction (BD), scanning direction (SD) and hatching direction (HD) coordination are also shown in Figure 1. The experiment was repeated three times, with the four cubes and four cuboids per print.
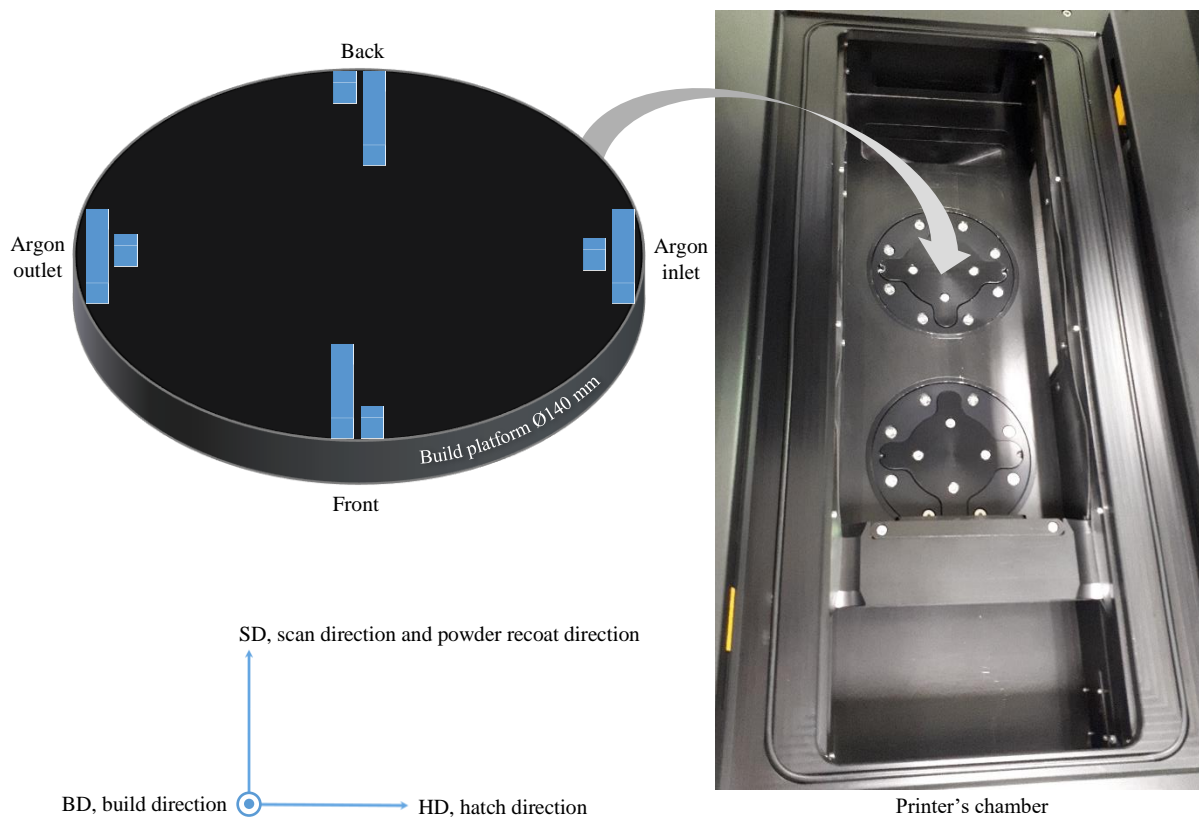

Figure 1 Illustration of built parts at the selected locations on the build platform.

2.2 Sample Characterisation

The printed cuboids were machined to dimensions according to the ASTM E8 standard and used for the tensile testing [30]. The cubes were used to assess the effect of location on the density, hardness, microstructure and corrosion properties of the samples. Archimedes density testing was performed in accordance with the ASTM standard B962 [31]. The measurements where conducted on a Sartorius YDK01 density determination kit coupled onto an Avery Berkel FA215DT density scale, where, deionised water (at room temperature) was used as the immersion liquid while determining the density. For robustness and cross checking of the measurement, the density of the printed samples was also measure with a Micromeritics AccuPyc 1330 helium pycnometer, where in each run the instrument reported the average density and standard deviation calculated from ten measurements. Prior to the hardness measurements and crystallographic analyses, the samples were ground with abrasive SiC papers and polished with 60 nm silica suspension, followed by ultrasonic cleaning in deionised water and drying with nitrogen gas. The Vickers hardness of the samples was measured using a Leitz microhardness tester and the measurements were performed according to ASTM E92 standard [32]. A nanoindenter (Bruker Hysitron TI Premier, USA) equipped with a standard Berkovich diamond indenter was used for nanohardness measurement of the samples. An array of sixteen nanoindentations was performed in the centre of each metallography sample with a 10 mN load (indentation depth around 300 nm) and intervals of 200 µm between indentations. The tensile test was performed using a Zwick Z050 (Zwick/Roell GmbH, Germany) computer-controlled tensile tester equipped with an Epsilon clip-on extensometer model 3542. A JEOL JSM-IT100 scanning electron microscope and a Keyence VHX2000E optical 3D digital microscope were used to obtain microstructural data. Crystallographic information about the samples was obtained using a triple-axis Jordan Valley Bede D1 high resolution X-ray diffraction system with a copper ($\lambda = 1.5405$ Å) radiation source operated at 45 kV and 40 mA, and a Zeiss Merlin field emission scanning electron microscope equipped with a EDAX/TSL EBSD system and a Hikari EBSD camera.

The electrochemical behaviour of the samples was investigated using a Gamry Reference 1000E potentiostat in a standard three-electrode cell. A saturated calomel electrode (SCE) and a high-density graphite rod were taken as the reference and the counter electrode, respectively, and the sample as the working electrode. Prior to electrochemical testing, the samples were ground with abrasive SiC papers and polished with 60 nm silica suspension, followed by ultrasonic cleaning in deionised water and drying with nitrogen gas. A surface area of 0.25 cm^2 was exposed to the electrolyte solution of 3.5% w/v NaCl H$_2$O during electrochemical testing. Initially, the working electrode was immersed in the electrolyte solution and kept at open circuit potential (OCP) for up to 2 hours for stabilisation, or until the potential variation was below 0.05 mV/s. Potentiodynamic polarisation behaviour was recorded at a scan rate of 1 mV/s, scanning from -0.5 V (vs. OCP) to an apex potential of 1.5 V (vs. OCP), or until the apex current density of 25 mA/cm^2 was measured during anodic polarisation, followed by a reverse scan back to 0.2 V (vs. OCP) at the same scan rate of 1 mV/s. Electrochemical impedance spectroscopy (EIS) was performed at OCP over a frequency ranging from 100 kHz to 10 mHz by applying a small alternating current perturbation of ±5 mV$_{rms}$. All electrochemical measurements were repeated three times. Electrochemical circuit modelling of the EIS data was performed using Gamry Echem Analyst version 7.8.2.

3. Results and Discussion

3.1 Effect of Part Location on Part Properties

3.1.1 Microstructure

The microstructure was characterised on the plane perpendicular to the build direction. Figure 2 shows that the laser meltpools were elongated along the laser scanning direction and that their geometrical features (formed patterns) varied according to their stabilities and surrounding conditions. Laser track meltpool anomalies such as inconsistencies Figure 2c and discontinuities Figure 2b could affect the crystallographic textures formed within the built part and the deformation mechanisms active in the deformation process, which could result in different mechanical properties. Porosity, which is a common defect in L-PBF processed 316L [33] was observed for all the samples as highlighted in Figure 2d. Here, the existence of porosity could be due to the stability, behaviour, and dimensions of the meltpools and the applied input parameters, in addition to related process phenomena and phase transformations that took place during printing. It was reported that failure of the meltpool to wet the surrounding material resulting from oxides at the side of the meltpool create regions of weakness and porosity [34]. Similarly, incomplete homologous wetting and solidification cause the molten material to have discontinuous propagation down with the previous layer which can result in spherical or irregular-shaped pores [35]. Porosity may also be formed when gases entrapped in the powder bed and powder particles dissolve in the meltpool and remain after solidification due to the high cooling rate [36]. Also, trapped within the solidified melt region, keyhole pores are formed when high enough energy densities are used. This is because the L-PBF welding regime changes from conduction (shallow and semi-circular meltpool shape) into keyhole mode (deep and narrow meltpool shape). Typically unstable, the keyhole mode can form pores due to metal vapour bubbles entrapped by solidification [37]. Meltpool instabilities appear at low laser scanning speeds in the form of distortions and irregularities, while excessively high laser scanning speeds give rise to the balling phenomenon. Balling, a manifestation of Plateau Rayleigh instability, can occur when the meltpool elongates and becomes unstable, breaking up into small islands [38]. Both, balling (small spherical balls) and laser splashed particles (spatter) decorating the building surface usually lead to the formation of irregular shaped pores.

The origin of defects in L-PBF is often related to the Plateau Raleigh capillary instability, Marangoni effect, vapour recoil pressure, Kelvin-Helmholtz hydrodynamic instability and external influences. The hydrodynamic instability of the meltpool known as the Kelvin Helmholtz hydrodynamic instability can cause humping (periodic occurrence of beadlike protuberances). Humping occurs when the velocity of the liquid metal at the top of the molten pool is lower than the inert gas velocity. This difference in velocities prompts the Kelvin Helmholtz hydrodynamic instability which occurs when the ratio of buoyancy force to shear force (Richardson number) is less than 0.25 [39]. The fluctuations of surface morphology can therefore lead to pore concentrations around the valleys. Resulting typically from the usage of very high laser scanning speeds and high laser powers, humping may greatly deteriorate the mechanical performance of printed components [40]. Similarly, insufficient heat input leads to lack of fusion defects. Figure 2b shows a lack of fusion void present in the microstructure of the argon outlet sample. It exhibits a high aspect ratio and preferred alignment with layer boundaries in the laser scanning direction. The formation of lack of fusion at the argon outlet could be related to argon flow separation and turbulences at this location. These could then increase the laser attenuation in response to the inert gas inefficiency in removing spatter and vapour plume emissions [41]. Consequently, reducing the depth and width of meltpools.

The microstructure of L-PBF processed 316L is fully austenitic and it has been frequently reported to consist of columnar grain structure [42,43]. The formation of columnar grains along the build direction is as a result of severe thermal gradient due to the heat sink of the previous layer. It can also be attributed to the formation of wider and shallower meltpools as a result of high laser power and decrease in cooling rate. The sample printed at the front of the build platform also exhibits banded grains grown through and perpendicular to meltpool boundaries, Figure 2a. As such the microstructure of elongated, banded grains, are particularly susceptible to intergranular corrosion. The severity of intergranular corrosion will depend on the extent to which grains elongated and banded, in addition to the continuity of the anodic path at grain boundaries [44–46]. On the other hand, the presence of banded grains in the sample can help to reduce brittleness as cracks moving through it may be deflected parallelly to the grains [47]. A recent study which obtained a similar grain structure to this study reported that the achieving of a high strain hardening rate was due to higher crystallographic texture dependent twinning [48]. Therefore, to some extent this finding can be related with the work hardening behaviour of the front location sample.
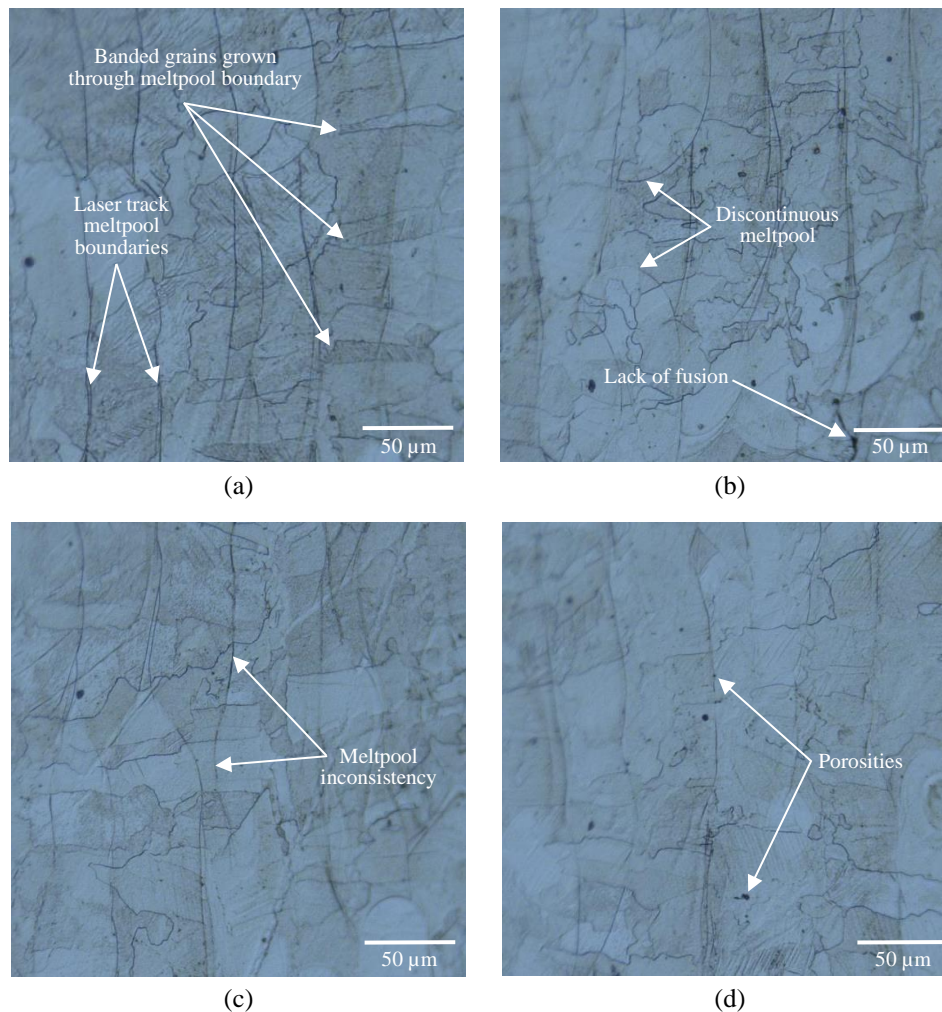

Figure 2 Optical micrographs showing microstructures at the: (a) front, (b) argon outlet, (c) back, and (d) argon inlet locations.

The samples were also investigated via electron scanning microscopy in order to obtain additional information about their microstructure. The common features observed in the samples are show Figure 3. Porosity defects were observed in all of the samples and this was found to be more pronounced in the argon outlet sample. The appearance of porosity defects was observed to be somewhat random within a given microstructure. Based on the clean nearby microstructure and the solidified molten boundaries around them it could be said that they emerged due to local instabilities in the molten metal track. Porosities with up to 20 µm in diameter were observed in the samples. However, most of the pores were spherical and <10 µm in diameter, suggesting gas entrapment during the solidification process. It is possible that the local instabilities in the molten region induced the deep or keyhole

mode in response to the evaporation of elements. This evaporation could then cause instantaneous volume expansion and produce pressure on the meltpools. Consequently, strong stirring and accelerated flow velocities in the liquid meltpools could have involved and strapped ambient gas. Therefore, when the recoil pressure became high and the surface tension become low, the gas bubbles descended near the bottom of meltpools. During this period, some gas bubbles could have escaped and others coalesced and trapped in the microstructure due to the fast cooling, which is a characteristic of the L-PBF process. Therefore, as the lifetime and depth of the keyhole mode meltpools are larger than that of the conductive mode meltpools, it could be said that the large pores within the microstructure of the samples are related to a local keyhole mode of melting. Interestingly, the back sample was the sample most affected by pores and these were rather elongated. An obvious explanation to this is the contamination of the powder bed in this region from spatter particles. Due to the alignment of the front sample with the back sample in the powder recoating direction, the collapsed spatter particles near the front sample were mixed with the virgin powder during the spreading of consecutive powder layers which then formed contaminated powder beds at the back sample location. In agreement with these results, Karimi et al. [11] reported a 20 % increased level of defects, mainly pores, in those samples printed near the corners of the build platform. To which, the formation of porosity was attributed to an existing higher cooling rate at these locations, accompanied by reduced liquid metal flow and shrinkage due to a lower specific volume of the solidified material than that of the melted material. Obeidi et al. [49] who also reported similar densities and microstructures to this work correlated the poor tensile performance of the samples to the keyhole pores and lack of fusion defects. It was noted in this work that the laser power and scanning speed play an important role in the development of such defects. Here, the fast solidification and cooling also induced the growth of very fine cellular structures within the microstructure of the manufactured samples, with cell widths of apparently only several hundred nanometers. According to the Hall-Petch relationship the strength of the material scales with the cell size [50]. While the elongation of the cells correlates to the progressive and steady strain hardening mechanism provided by the abundant and complicated interactions between dislocations and cells [51–53]. Therefore, the existing cell structures had a positive contribution to the mechanical properties of the samples. This is in agreement with the literature which reports cellular structures led-improvements in yield strength, hardness and fatigue performance [54–56]. Micrographs representing larger surface areas of the printed samples are available in the supplementary material.
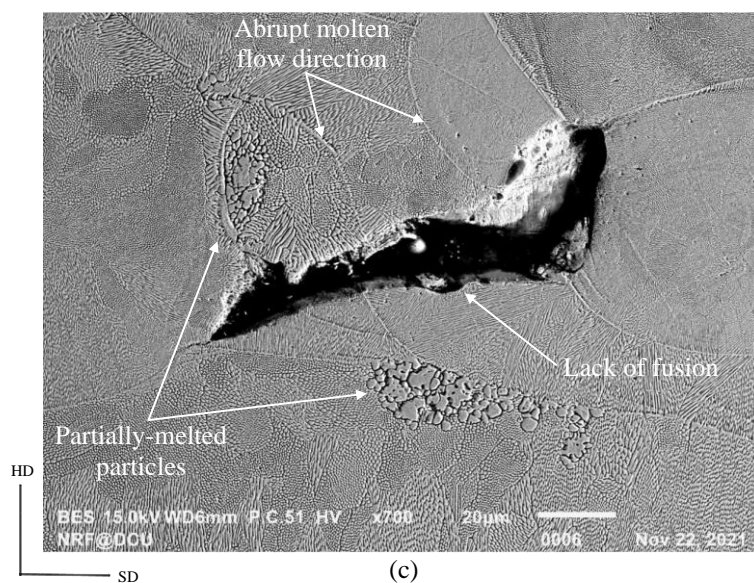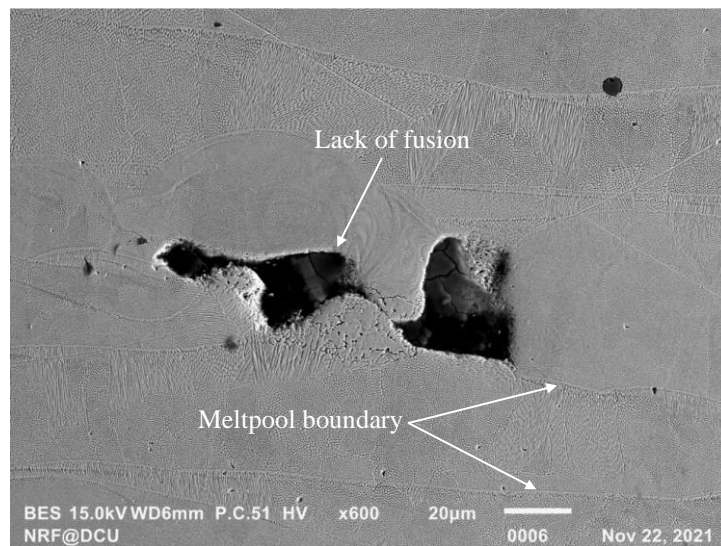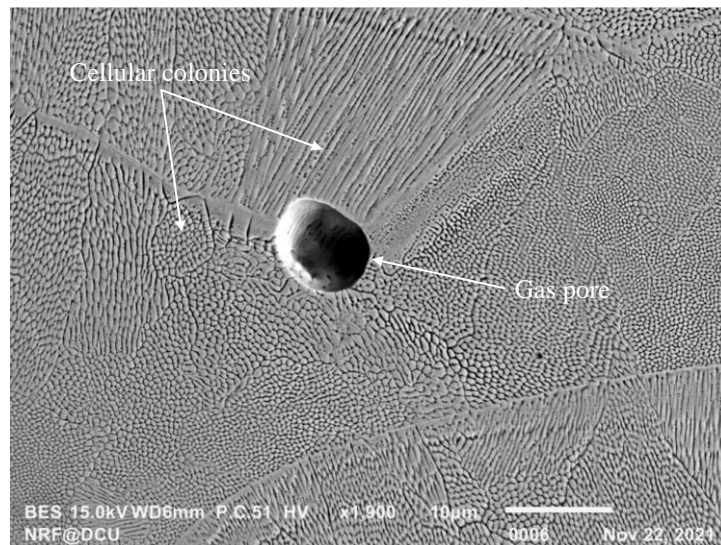
(a)

(b)

(c)

Figure 3 Backscattered electron micrographs showing the lack of fusion and porosity defects and the existence of subgrain cellular structures in the microstructure of the samples.

3.1.2 Grain Size

The effect of the build location parameter on grain size is contrasted in Figure 4. The grains morphology and their spatial distribution can be visualised in the grain maps available in the supplementary material. The results show a trend in the relationship between the average grain size and the sample print location, in which, two distinct grain size groups exist. The front and back locations led to the growth of several coarse grains (>45 µm). In contrast, the argon outlet and argon inlet locations led to the growth of relatively finer grains. Clearly, the high alignment of the argon outlet and argon inlet samples with the flowing argon stream, see Figure 1, resulted in a slightly higher cooling rate. Consequently, grain size became relatively uniform and finer. As all of the four samples were printed in the same build and using the same input processing parameters, one would hypothesise the build location to have no effect on grain size. However, the results showed that the location parameter plays a contributing role to grain refinement. Additionally, despite the observed grain size refinement being only 2 µm, when considering all the resulting microstructure features together, the final mechanical performance of each individual sample can be different.

In the literature, the Hall-Petch equation expresses that the hardness increases as $1/\text{grain size}^{0.5}$ [57]. This means that smaller grain-sized material is harder. In a harder material, higher applied stresses are required to propagate dislocations through it, which is the case for small grain-sized materials, where the role of the grain boundaries in preventing dislocation propagation becomes progressively pronounced, leading to increased stress concentration at grain boundaries due to dislocation pile up.
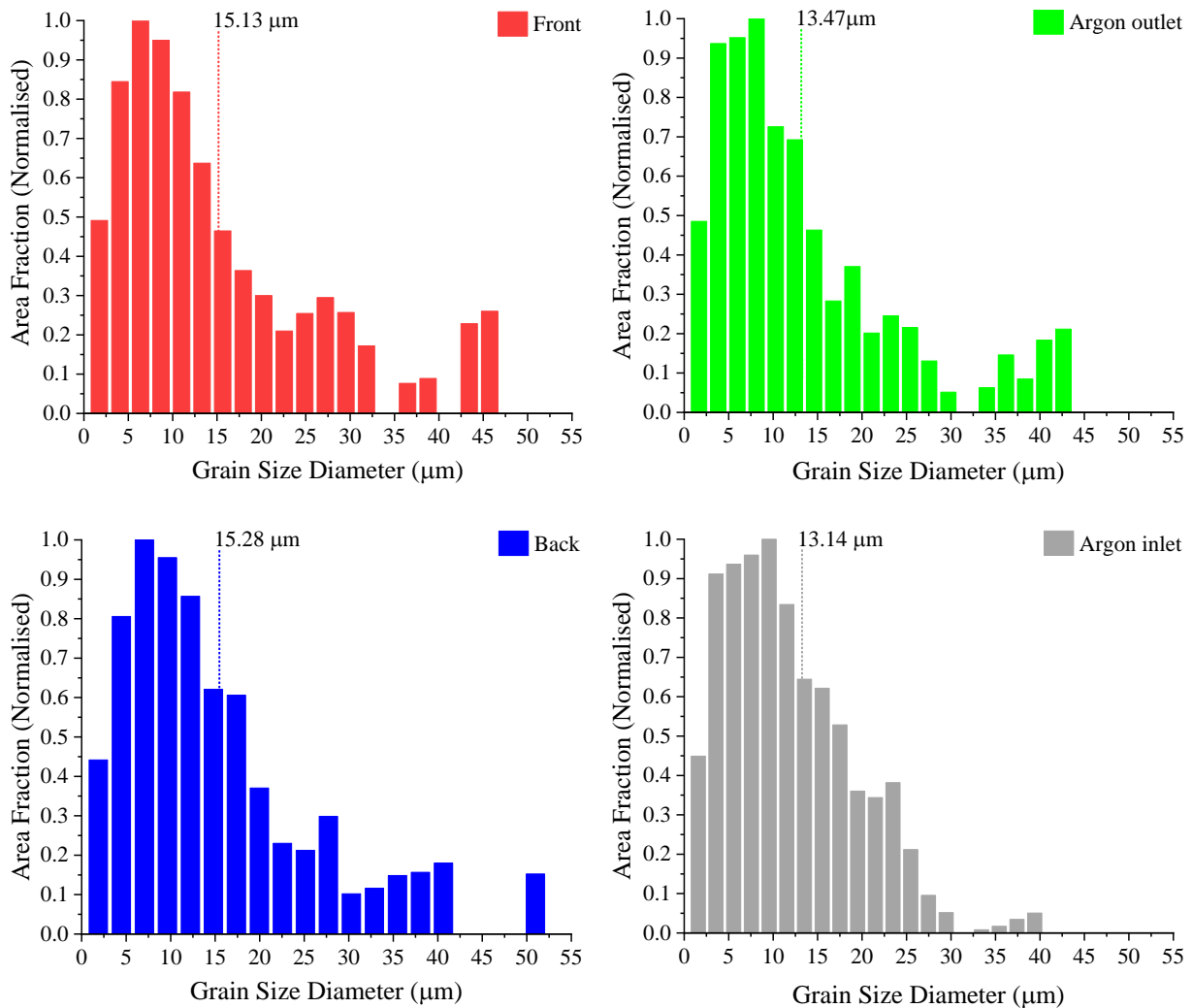

Figure 4 Electron backscatter diffraction quantitatively measured grain size distribution contrasting the effect of sample build location.

3.1.3 Density

Density is an important physical property influencing the mechanical integrity of parts. Hence, it is used as a measure of part quality [58]. In L-PBF, the density of parts is generally discussed as being influenced by the laser and scanning parameters which can lead to defects in the part such as lack of fusion, voids and pores [59,60]. The study presented here indicates that part density is also influenced by the part build location. In order to properly assess the influence of the build location on part density, the density of the 316L powder used to print the samples was measured via helium pycnometry. The measured powder density of 7.82 g/cm^3 was then assumed to be the true density of the 316L. Table 1 shows that part density varies substantially throughout the build space. The highest density was measured for those parts printed at front and the lowest density was measured for those parts located near the argon outlet. There are various contributors to density anisotropy within the build space. However, here, the main contributors were the powder bed packing density and the process by-product known as spatter. Particle size segregation takes place along the powder recoating direction, therefore, from the front to the back location. At the front, finer particles contained in the powder ensures a higher powder bed packing density at this location [26,61]. At the back, there exists a lower packing efficiency due to the lack of fine particles and so voids are left between the coarser particles [26,62]. One of the functions of the argon flow is to prevent in-flight spatter from collapsing onto the build platform. The likelihood that some spatter will collapse onto a building surface located near the argon outlet is much higher than that of the argon inlet. Therefore, the difference in density between the parts located near the argon inlet and argon outlet is predominantly due to a spatter-induced defect within the bulk part. Spatter is detrimental and its formation should be minimised [17]. Furthermore, the results indicated that a higher powder bed packing density is key to achieving higher part densification.

Table 1 The density of the samples with respect to their printing location on the build platform. The uncertainty was estimated with a 95% confidence interval.

Sample	Archimedes method (g/cm^3)	Helium pycnometry (g/cm^3)
Front	$7.48_{\pm 0.034}$	$7.40_{\pm 0.030}$
Argon outlet	$7.07_{\pm 0.060}$	$7.00_{\pm 0.035}$
Back	$7.31_{\pm 0.020}$	$7.30_{\pm 0.018}$
Argon inlet	$7.37_{\pm 0.036}$	$7.35_{\pm 0.027}$

3.1.4 Microhardness

It is evident that the location also has an influence on the samples microhardness, seen Figure 5. Parts printed near the argon outlet are more liable to internal defects. However, as the highest hardness was measured at those parts printed near the argon outlet it is possible that the microstructural characteristics of the samples varies with the location. Therefore, the observed discrepancies in hardness may be attributed to different grain size and texture induced by the location parameter. One big player to this is the argon flow as it influences the cooling rate and cooling direction depending on the part location.
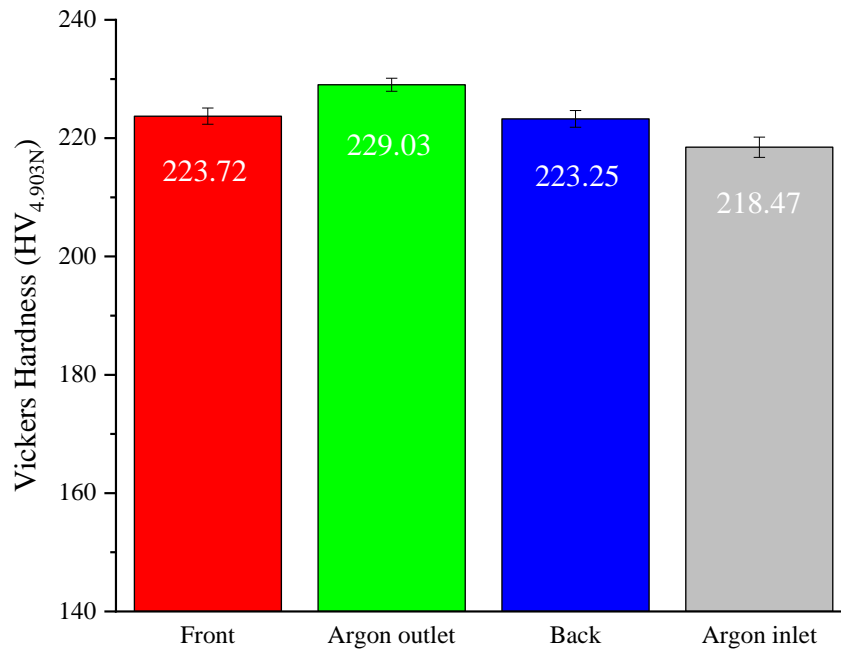
Figure 5 Microhardness of the printed samples with respect to part location on the build platform. The uncertainty was estimated with a 95% confidence interval.
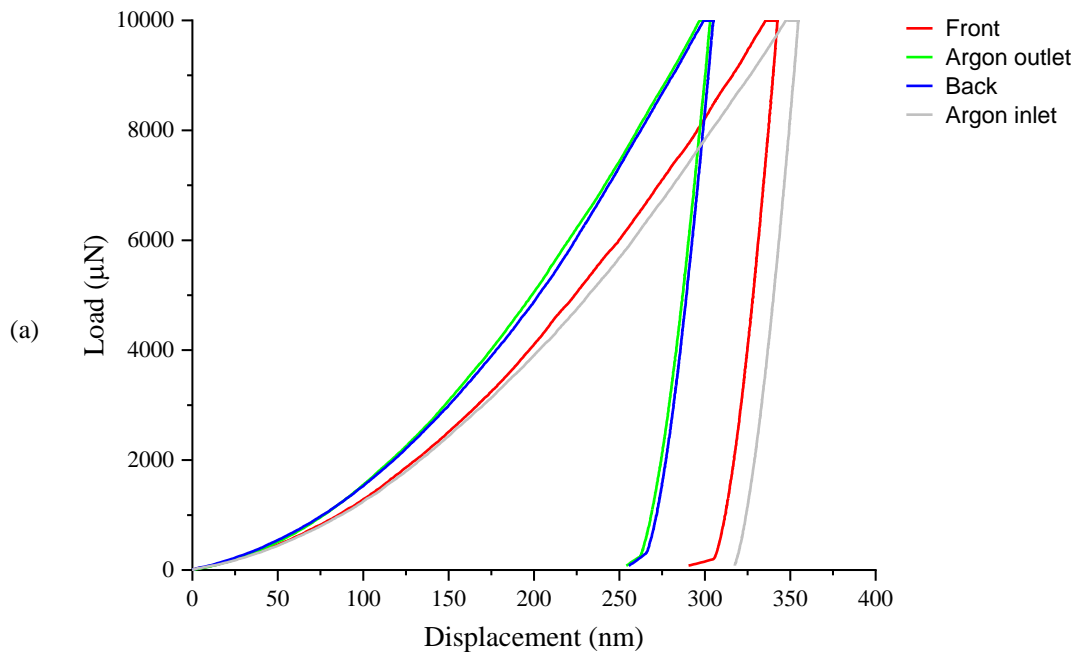
3.1.5 Nanohardness

Figure 6 shows the nanoindentation load-displacement curve and the measured nanohardness, reduced modulus and the calculated nanoindentation parameters of the printed samples. The load-displacement curves depict an elastic-plastic deformation behaviour. It was observed that the sample located near the argon inlet showed the largest penetration depth. The argon outlet and back samples showed similar load-displacement curves and a higher resistance to plastic deformation, which implies a higher hardness and stiffness. The nanohardness values are aligned with the microhardness results. Both indicate the highest hardness on the sample located near the argon outlet and the lowest hardness on the sample located near the argon inlet. It was reported elsewhere and it is in this case possible that there is a dependence of hardness on crystal orientation [63]. The results of the crystallographic analysis will be presented and discussed in section 3.1.6. The reduced modulus E_r obtained from the nanoindentation test represents the elastic deformation that occurs in both sample and indenter tip [64]. The indentation modulus E is comparable with the Young's modulus of the material and it can be expressed as:

$$E = \frac{(1 - v^2)}{\frac{1}{E_r} - \frac{(1 - v_i^2)}{E_i}}$$

where v is Poisson's ratio for the sample, E_i and v_i are the elastic modulus and Poisson's ratio for the indenter. For the Berkovich diamond indenter, the values of E_i = 1140 GPa and v_i = 0.07 are frequently used [65] and the possion's ratio of L-PBF processed 316L was taken as 0.25 [66]. The calculated Young's modulus for the front, argon outlet, back and argon inlet samples are 220.46, 225.88, 222.43 and 203.79 GPa, respectively. These results indicate that the nanohardness tends to increase with an increase in Young's modulus. The elastic and plastic behaviour of the samples were further assessed from the nanoindentation results by evaluating the elastic recovery index (W_e/W_t) and plasticity index (W_p/W_t). The elastic recovery index provides information about the energy released from the material under mechanical loading, while the plasticity index provides information about the intrinsic plastic behaviour of materials [67,68]. Although material hardness is a crucial parameter controlling wear, other parameters in the nanoscale such as the ability of a material to resist elastic strain (H/E_r) and the material's resistance to plastic deformation in loaded contact (H^3/E_r^2) are also used to understand the wear behaviour of materials [69,70]. The highest elastic recovery index was obtained for the argon outlet sample and the lowest for the argon inlet sample, see Figure 6c. Here, a general correlation between hardness and elastic recovery index exists, where elastic recovery index increases with increasing hardness. The argon inlet sample showed the largest intrinsic plasticity, which implies that it experienced the least hindrances to plastic deformation owing to its higher ductility. From the results, it is observed that the argon outlet and back samples depict the

highest resistance to elastic strain to failure. This suggests that these samples can allow redistribution of the load over a larger zone and thus lead to a delay in surface failure. Figure 6c also shows the effect of printing location on the (H^3/E_r^2) parameter. It indicates that the argon outlet sample has higher wear resistance to wear caused by gradual removal of material driven by plastic deformation. It is observed that the elastic recovery index, resistance to elastic strain and the resistance to plastic deformation of the samples are directly proportional; they also follow the same trend as the nanohardness and reduced modulus. For some metals like stainless steels, the strength of a material is related to its hardness and a material with higher hardness retains a higher strength [71]. From the reported nanoindentation parameters, it can be said that discrepancies between samples may be ascribed to differences in the microstructure, as a smaller measured grain size is related to a high hardness [72].

(a)

(b)

Location	Nanohardness (GPa)	Reduced Modulus (GPa)
Front	$3.42_{\pm 0.14}$	$195.11_{\pm 4.28}$
Argon outlet	$4.46_{\pm 0.22}$	$199.07_{\pm 3.26}$
Back	$4.38_{\pm 0.31}$	$196.55_{\pm 6.08}$
Argon inlet	$3.17_{\pm 0.07}$	$182.71_{\pm 3.48}$

(c)

Location	W_e/W_t	W_p/W_t	H/E_r	H^3/E_r^2 (MPa)
Front	0.121	0.879	0.018	1.05
Argon outlet	0.153	0.847	0.022	2.24
Back	0.150	0.850	0.022	2.18
Argon inlet	0.115	0.885	0.017	0.95

W_e, W_p and W_t indicate recoverable elastic work, residual plastic work and total work [73,74].
H and E_r indicate nanohardness and reduced modulus, respectively.

Figure 6 Nanoindentation data: (a) load-displacement curve, (b) measured nanohardness and reduced modulus and (c) calculated nanoindentation parameters of the printed samples. The uncertainty was estimated with a 95% confidence interval.

3.1.6 Tensile Properties

The tensile performance of the samples based on their location is presented in Figure 7. Similar tensile properties were obtained from the front, back and argon inlet samples, however, the highest yield strength as well as the highest ductility were both found in the argon inlet sample. It was reported that grain refining increases yield

strength while also improving toughness [75–77]. Therefore, in the case of the argon inlet sample, the strengthening occurred through the increase in grain boundary area. This would make crack propagation more difficult, as to go across a fine grained material, a crack would require to be initiated in and cross over many grains. This would require a great amount of energy and consequently raising the energy to fracture. The negative effect of the argon outlet location on the tensile properties is clear from Figure 7a and Figure 7b. The inferior tensile strength of the argon outlet sample could be due to several factors such as microstructure, crystallographic texture and porosity. It was reported that low elongation to failure could be attributed to a combination of factors such as dislocation pileup at grain boundaries and the presence of irregularly shaped defects like lack of fusion porosity [78]. Poor elongation to failure is most likely attributed to the presence of lack of fusion defects. The presence of such defects having a high aspect ratio oriented perpendicularly to the uniaxial testing direction could act as stress concentrators, therefore leading to a decrease in tensile ductility. The argon outlet location is the location on the build platform most affected by spatter [79]. In L-PBF, spatter residing near or onto a building surface can alter powder redistribution, cause agglomerations, contamination and loss of powder, which are known to contribute to defect formation.

In order to understand the work hardening behaviour of the samples, the instantaneous strain hardening rate was considered. Kocks-Mecking plot illustrating strain hardening rate ($\theta = d\sigma/d\varepsilon$) as a function of net flow stress ($\sigma - \sigma y$) is depicted in Figure 7c. In polycrystals, stage I hardening is absent and stage II hardening often degenerates into a low strain limit that is athermal [80,81]. Stage I hardening depends strongly on the crystal orientation and if deformation takes place through multiple slips it might not be observed. Stage II hardening is governed by the interaction of dislocations belonging to the primary slip system with those moving through the intersecting slip system [82]. Both of these stages were missing in the present investigation. The samples exhibited instead a different type of two-stage work hardening behavior, Stage III and IV. This is shown by a distinct sharp decline in strain hardening rate (transient stage) followed by a gradual nearly linear decrease at high stresses (stage IV hardening). At the elastoplastic transition, Stage III hardening, the strain hardening rate underwent a drastic reduction. While at the dislocation storage process, stage IV hardening, it was observed a nearly constant strain hardening rate [83]. The higher strain hardening rate of the front and argon outlet samples in the early stages of deformation can be attributed to a higher rate of primary twinning formation and twin density. The favorable effect of twinning on strain hardening capacity at stage IV hardening of the argon inlet region could be related to the the dynamic Hall-Petch effect of reduction of the dislocation mean free path, as twin boundaries provide high energy obstacles to dislocation glide. This inferred influence from the results presented herein from the microstructure and the texture has been noted previously [84,85].

(a)
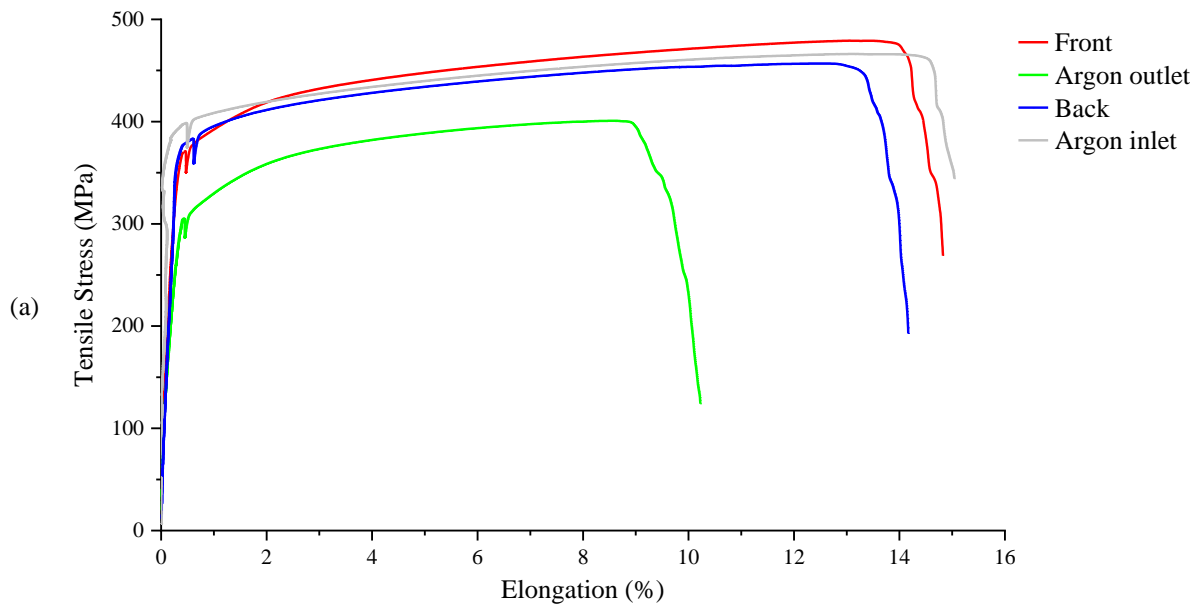
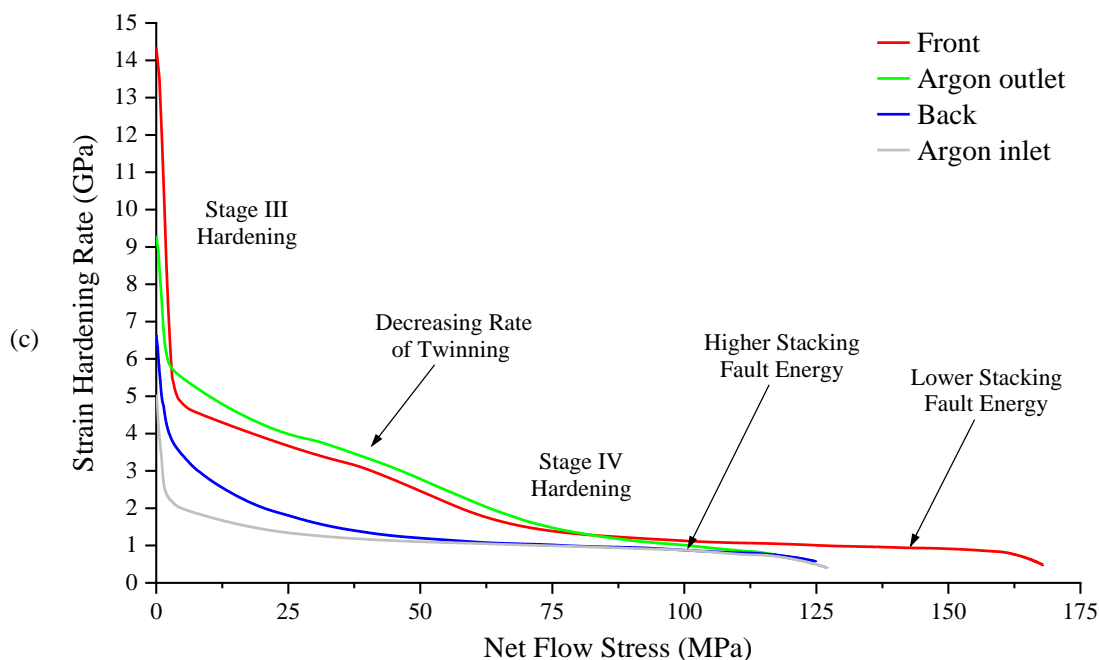| Location	Modulus of Elasticity (GPa)	Tensile Strength, Yield (MPa)	Tensile Strength, Ultimate (MPa)
Front	$146.49_{\pm 2.99}$	$393.89_{\pm 27.57}$	$475.83_{\pm 21.59}$
Argon outlet	$129.61_{\pm 3.00}$	$293.42_{\pm 9.29}$	$344.46_{\pm 41.91}$
Back	$140.21_{\pm 5.22}$	$381.25_{\pm 39.14}$	$458.38_{\pm 37.95}$
Argon inlet	$144.77_{\pm 4.32}$	$403.63_{\pm 6.47}$	$459.01_{\pm 11.79}$

(b)

(c)

Figure 7 (a) tensile curve of samples printed at critical locations, (b) their respective tensile properties and (c) Kocks-Mecking analysis of work hardening. The uncertainty was estimated with a 95% confidence interval.

3.1.7 Crystallography

A comparison of the X-ray diffraction patterns for the samples is shown in Figure 8. The face-centered cubic peaks (111), (200), (220) and (311) corresponding to the crystalline austenite phase were identified and verify with previous results in the literature [86,87]. A considerable change in relative intensities was observed in all samples, mainly through the (111) and (200) peak intensity distribution. This suggests the presence of different

crystallographic texture effects between samples generated by the location parameter. The X-ray peak broadening could be due to lattice defects such as microstrains, crystallite sizes and process-induced dislocations [88]. Similarly, the diffraction line shifts, noticeable from the 2θ angles listed in Table 2, could be a result of stress imbalance at grain boundaries and spatter induced composition changes introducing foreign atoms in the lattice, hence changing the lattice size.
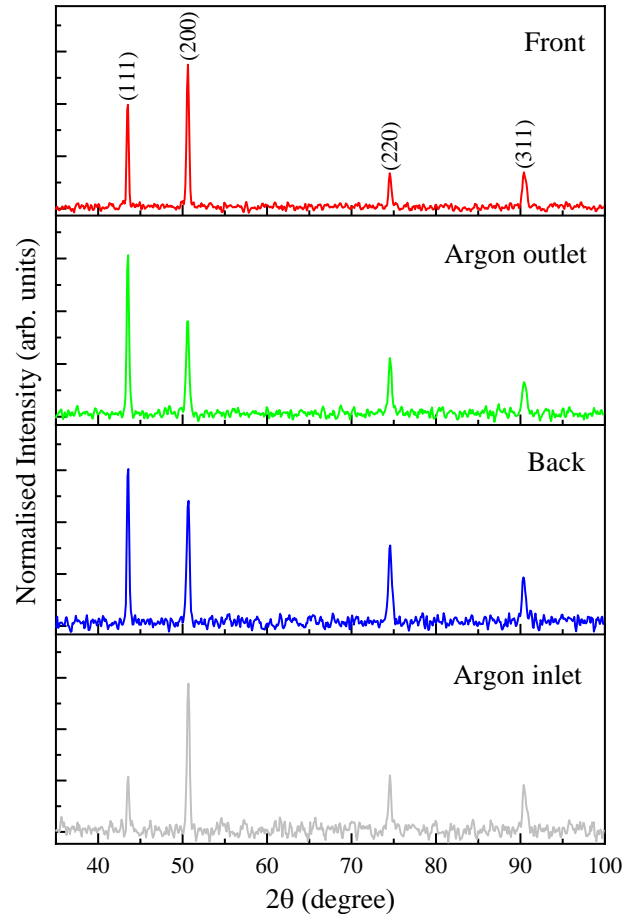

Figure 8 X-ray diffraction spectra of the printed samples in dependence of the part location on the build platform.

The stacking fault energy represents the barrier level for the dissociation of a perfect dislocation into Shockley partial dislocations and the susceptibility for formation of stacking faults [89–91]. Partial dislocations are known to play unique roles in twinning, phase transformations and formation of dislocation barriers. Hence, the stacking fault energy is an important parameter to determine the deformation schemes. Here, the stacking fault probability (P_{sf}) and root mean square microstrain $(\langle\varepsilon_{50}^2\rangle_{111})$ were determined by analysing the X-ray diffraction peak profiles as described in reference [92]. Then, the stacking fault energy was calculated using the well-established Reed and Schramm's relationship [93].

$$Stacking\ fault\ energy = \frac{6.6\ a_0}{\pi\sqrt{3}} \left(\frac{2C_{44}}{C_{11} - C_{12}}\right)^{-0.37} \frac{\langle\varepsilon_{50}^2\rangle_{111}}{P_{sf}} \left(\frac{C_{44} + C_{11} - C_{12}}{3}\right)$$

where a_0 is the lattice parameter, and the elastic constants C_{11}, C_{12} and C_{44} of stainless steel AISI 316L were adopted from reference [94]. The calculated stacking fault energies are shown in Table 2 for the respective part locations. All the samples presented similar and relatively low stacking fault energy of ~25 mJ/m^2, which favours deformation-induced twinning. In general, it has been known that the stacking fault energy varies depending on temperature, concentration of alloying elements, grain size and strain. In fact, during tensile testing, the stacking fault energy decreases with increasing strain [95–97]. Where this is associated with deformation activity changes from dislocation slip to twinning as straining. Based on this and on the results seen until now and also knowing that low stacking fault energy relates to high strain hardening rate, the higher strain hardening rate of the front

sample seen in Figure 7c can be attributed to a longer twinning period due to much earlier manifestation of the critical resolved shear stress for twinning, in addition also to possibly larger amounts of stacking faults which increase the stacking fault probability, consequently causing the decrease of the stacking fault energy.

Table 2 X-ray diffraction data, interplanar spacing and stacking fault energy of the printed samples.

Sample	(hkl)	2θ (degree)	FWHM (degree)	d-spacing (nm)	Stacking Fault Energy (mJ/m^2)
Front	111	43.493	0.140	0.208	24.833
	200	50.619	0.173	0.180	
	220	74.552	0.189	0.127	
	311	90.479	0.313	0.108	
Argon outlet	111	43.519	0.160	0.208	25.198
	200	50.593	0.209	0.180	
	220	74.573	0.214	0.127	
	311	90.471	0.330	0.108	
Back	111	43.535	0.154	0.208	24.658
	200	50.651	0.205	0.180	
	220	74.570	0.243	0.127	
	311	90.396	0.248	0.109	
Argon inlet	111	43.542	0.160	0.208	24.652
	200	50.672	0.183	0.180	
	220	74.544	0.158	0.127	
	311	90.401	0.284	0.109	

During the L-PBF processing of 316L, columnar grain growth is determined by heat flow direction and influenced by the process input parameters. Within the columnar grains, cellular structures tend to grow perpendicularly to the liquid-solid interface regardless of crystal orientation. However, when the growth rate increases then the direction of cell growth diverges towards the preferred crystallographic growth direction. Therefore, it is important to determine the influence of the location parameter on crystallographic texture in order to understand the mechanical behaviour of the printed samples.

Typically, in L-PBF columnar grains grow elongated along the build direction [98]. Therefore, when viewed from the plane normal to the build direction, depending on the applied scanning strategy, grains can exhibit equiaxed, banded and or irregular faceted morphologies [99–101]. Figure 9 presents electron backscatter diffraction maps contrasting the effect of sample build location on grain orientation. With reference to the inverse pole figure colour coded map, it can be seen that the crystallographic orientation of the samples is mainly in the <001> orientation. However, the argon outlet and argon inlet samples showed a higher number of grains oriented between <001> and <101> (yellow coloured). As the location of these two samples was perfectly aligned with the flowing argon stream, they possibly experienced a higher cooling rate and so a higher horizontal cooling gradient. It is also worth mentioning that the formed and seen grain patterns resulted from the applied scanning strategy. Additionally, as it is observed, the applied 50 % hatch translation per layer play a major role in grain downsizing and grain size uniformity.
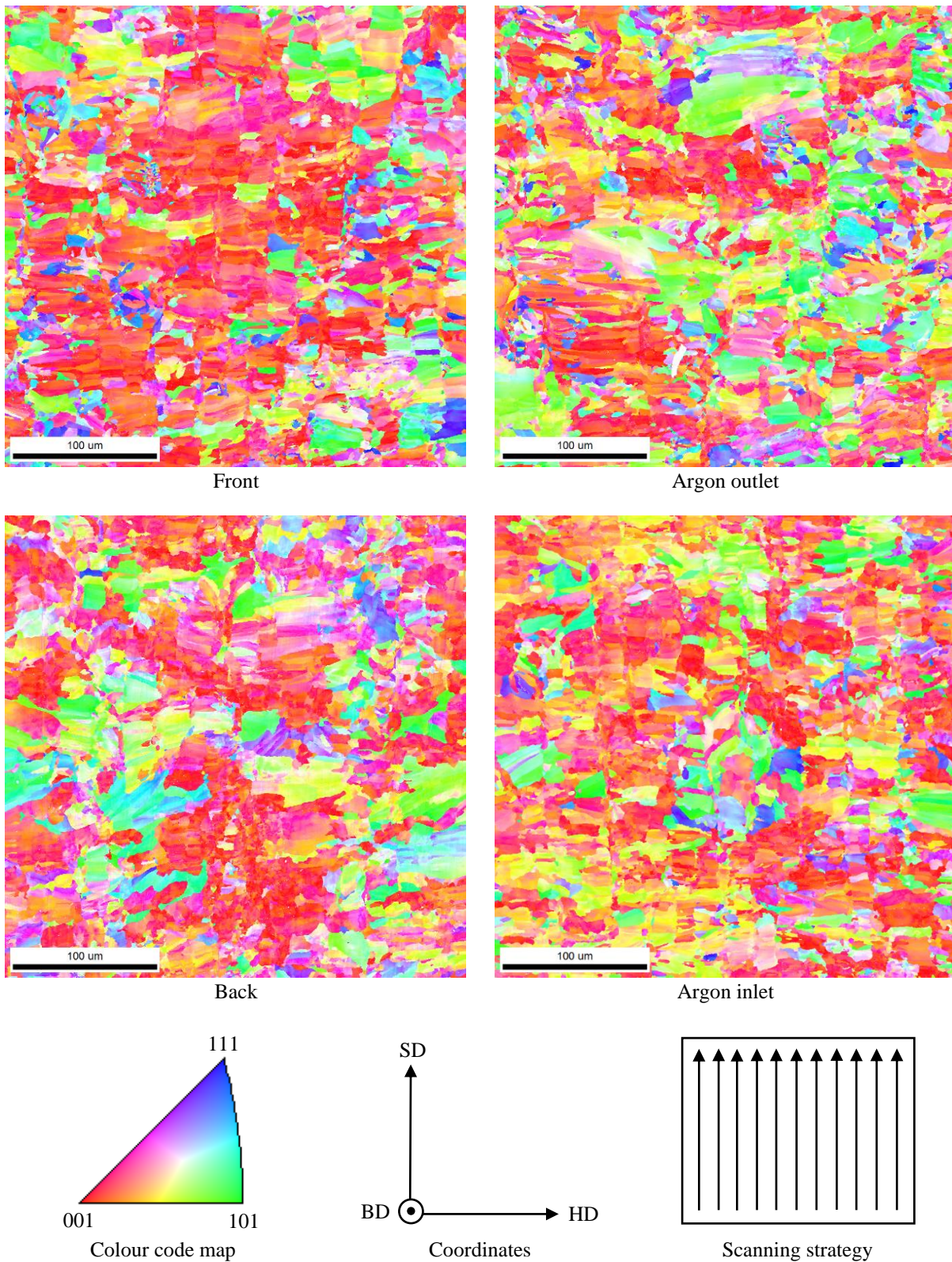
Figure 9 Electron backscatter diffraction maps contrasting the effect of sample build location on grain orientation.

The crystallographic textures resulting from the build location parameter are depicted in Figure 10. All four locations exhibited a very sharp <001> cube texture, indicating that many of the grains were aligned with reference to the samples build direction. However, it is worth to note and compare the maximum intensity of the colour scale bars corresponding to the representative pole figure of the samples. Although the texture was qualitatively similar in the four samples, the lower intensity of the argon outlet pole figure indicates that the argon outlet sample

had inferior crystallographic anisotropy in comparison for example with the argon inlet sample. Therefore, as the argon outlet sample showed the highest hardness and lowest yield strength and the argon inlet sample the lowest hardness and highest yield strength, it can be concluded that location parameter slightly altered the crystallographic anisotropy, and hence contributed to the seen discrepancies between the samples mechanical performance.
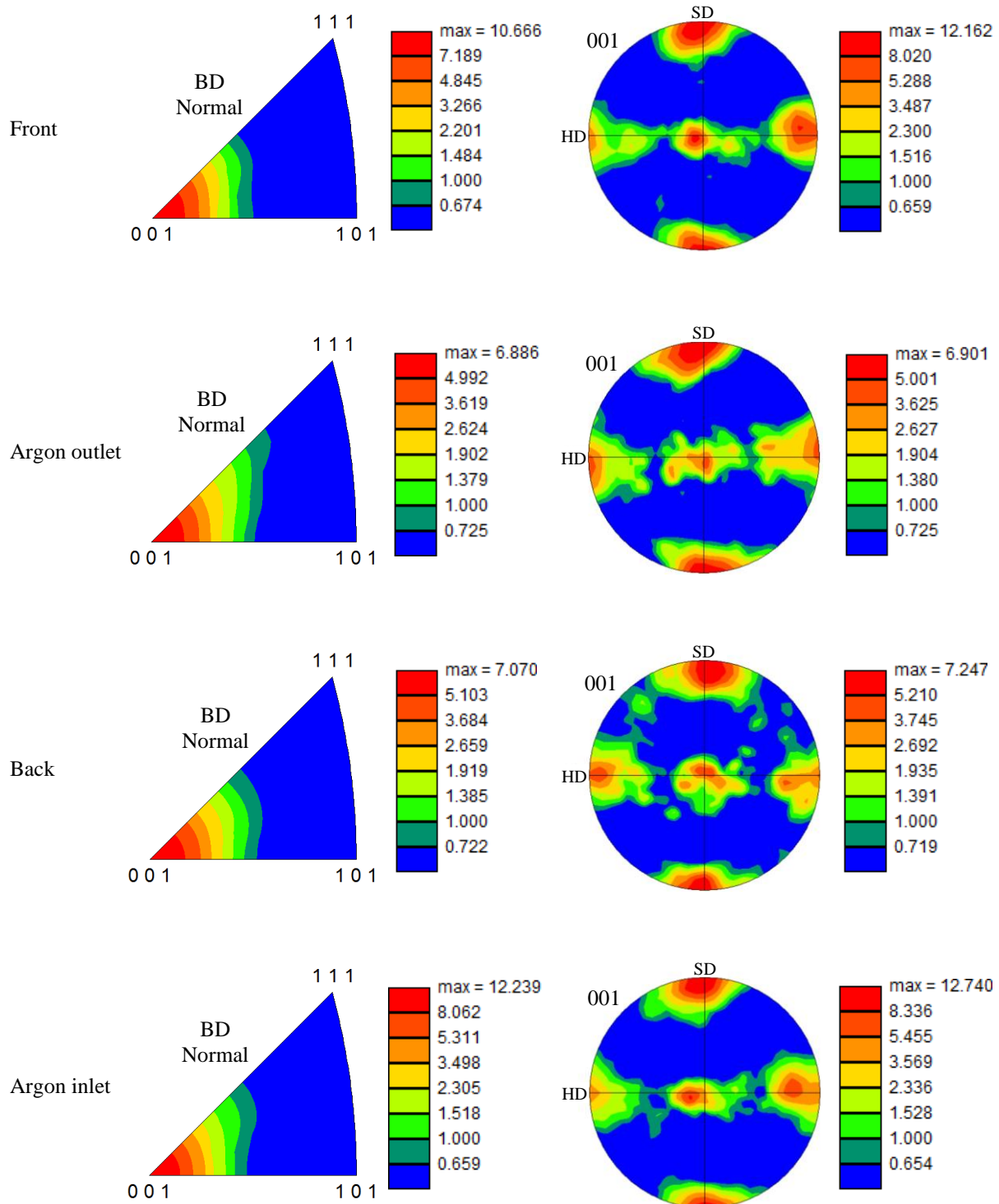

Figure 10 Crystallographic textures resulting from the build location parameter.

Figure 11 shows the changes in grain boundary misorientation angle due to the location parameter. The red line represents the low angle grain boundaries (LAGBs) (<10°) and the blue line represents the high angle grain

boundaries (HAGBs) (≥10°). Figure 11 also tabulates the fraction of LAGBs and HAGBs in the samples. A salient feature of L-PBF processed 316L is the existence of a large fraction of LAGBs [50]. However, here, it is observed an equal fraction of LAGBs and HAGBs in the argon outlet misorientation map. In contrast, the back sample exhibited a high fraction of LAGBs. It is also worth noting the presence of a large number of LAGBs between the meltpools boundaries, and that the LAGBs and HAGBs are not uniformly distributed in the microstructure of the samples. It appears that these were due to the cyclic local high heating and cooling and the thermal constraint with the previously processed layer, which then developed uneven residual stress in the microstructure [102]. Consequently, grains with large residual stress accommodated the strain and produced local orientation and <2° angle grain boundaries. Considering the results presented in Table 1 and Figure 7 and knowing that the ductility decreases as a result of defects such as porosity, it can be observed a relationship between the crystallographic misorientations and the mechanical performance of the samples. Samples with large fractions of LAGBs showed higher yield strengths. This was because the LAGBs hindered dislocation motion during the tensile deformation, hence strengthening the samples. However, in comparison to the cellular structures (Figure 3), the respective contribution of LAGBs to the yield strength was much lower [50,103]. Additionally, cellular boundaries with high dislocation densities could have acted as HAGBs during the deformation and so resulted in grain boundary strengthening. Conversely, cellular boundaries with low dislocation densities could have enhanced the deformation twinning and contributed to the ductility of the samples. The local variation in misorientation observed through kernel average misorientation maps and distributions was used to evaluate the residual strain and dislocation density in the samples which are presented next.
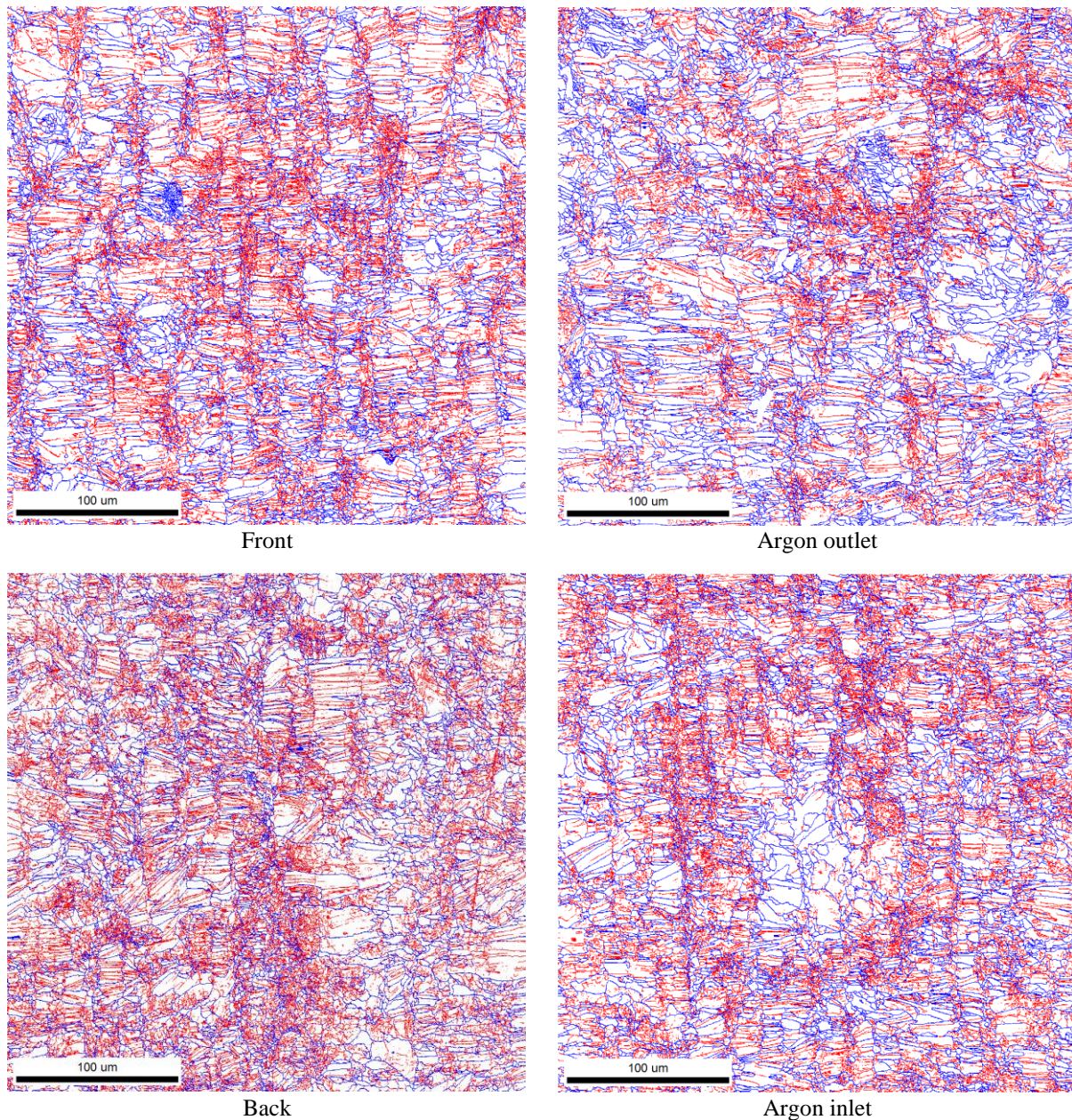
Sample	—— LAGBs (<10°)	—— HAGBs (≥10°)
Front	0.58	0.42
Argon outlet	0.50	0.50
Back	0.64	0.36
Argon inlet	0.59	0.41

Figure 11 Grain boundary maps obtained by electron backscatter diffraction contrasting the fraction of low angle and high angle grain boundaries in the samples.

The kernel average misorientation of the samples is shown in Figure 12. The front, argon outlet and argon inlet samples exhibited similar distributions of kernel average misorientation. However, the back sample developed a relatively high kernel average misorientation, with an average value of 0.84°. An increase in the angle of kernel average misorientation is usually related in the literature to low laser input energies [104–106]. Therefore, contrary to the aforestated, heat accumulation resulting from high laser input energies can lead to an in-situ relaxation heat treatment that reduces the amount of strain and dislocations in the material. Accordingly, it is possible that the observed kernel average misorientation in the front sample resulted from laser attenuations in response to the inert gas flow separation and turbulences at this location, and from local multiple thermal cycles due to meltpool

fluctuations. Additionally, the degree of local misorientation seemed also depend on the crystal orientation. This was confirmed in the pole figure of the back sample (Figure 10), as in this sample, several grains grew oriented between the scanning and hatching direction. Therefore, the resultant kernel average misorientation in the back sample was driven mainly by the processing conditions at the back location and the local microstructure. Moreover, the results suggested that microstructures having more dominant textures would accumulate lower amounts of kernel average misorientation, therefore increasing the residual stress relaxation effect.
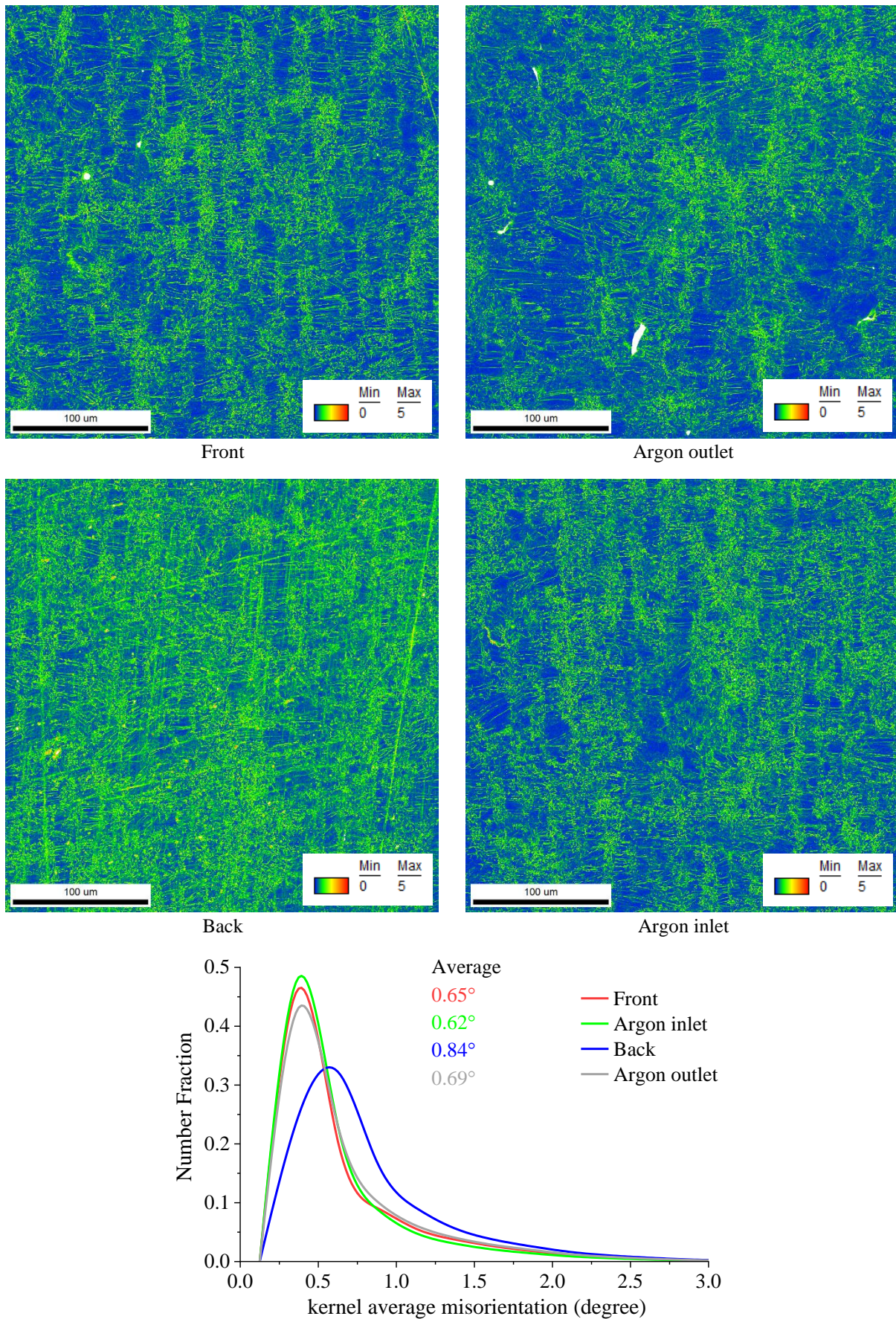
Figure 12 Kernel average misorientation maps and angle distributions corresponding to the 316L samples printed at critical locations on the build platform.

3.1.8 Corrosion

The dynamic corrosion behaviour of the samples to 3.5% w/v NaCl H_2O (pH = 8.2) electrolyte solution captured by potentiodynamic polarisation is presented in the voltammograms of Figure 13a and the relevant parameters extracted from the polarisation curves are presented in Figure 13b. The argon outlet and back samples show a passivation-like curve (active-passive behaviour) [107]. Where a distinctly diminished passive span can be observed, revealing that passivation was unstable. The presence of pores in the samples could affect the formation of the protective passive film while polarising. For example, by forming a porous thin or non-uniform film which can be easily penetrated, hence accelerating corrosion. Furthermore, because of the existence of an abnormal film, localised corrosion could manifest as contribute to anodic current via oxidation of the surface within the pores. Additionally, the observed ever increasing current during anodic polarisation is a clear indication of the formation of a defective oxide film. The polarisation curve of these two samples also shows a slightly lower passivation current density for the back sample, suggesting that the passive film is relatively easier to form. As seen in Figure 13a, the front and argon inlet samples both exhibited noticeable pseudo passivity, therefore suggesting that stable pitting sites (localised corrosion) were formed during the OCP measurements. The observed pseudo passivation resulted from the formation of a non-protective oxide film. This implies that the surfaces were only partially passivated and that active pitting sites were already initiated at potentials lower than the pseudo passive potential spans. Above the pseudo passive span, the contribution of pitting to the total current becomes significant and resulted in an increasing current density with the increasing potential. The extracted polarisation parameters presented in Figure 13b show that the front sample exhibited the noblest corrosion potential (-205.00 mV), followed by the argon inlet sample (-267.33 mV) which then exhibited the lowest corrosion current density (0.48 $\mu A/cm^2$). Therefore, the argon inlet sample demonstrated higher corrosion resistance than the other three samples. Additionally, the argon inlet sample also showed a lower corrosion rate (0.80 mils per year, mpy) [108]. This could be due to dissolution of iron and chromium oxides/hydroxides in the presence of the electrolyte forming stable complexed species already at OCP window prior to anodic polarisation [109].

(a)
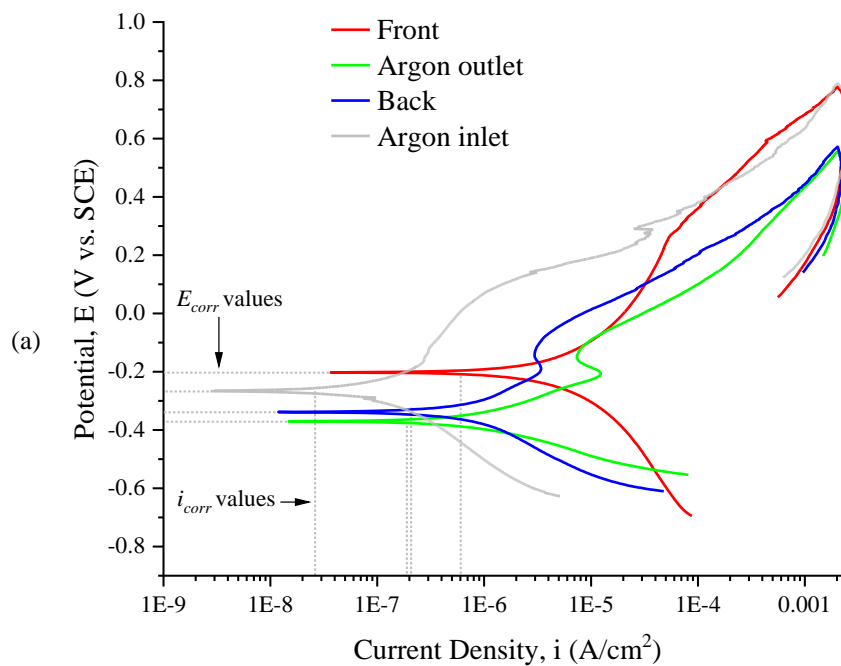
Location	E_{corr} (mV)	i_{corr} ($\mu A/cm^2$)	CR (mpy)
Front	$-205.00_{\pm8.29}$	$29.90_{\pm1.15}$	$41.11_{\pm1.98}$
Argon outlet	$-365.00_{\pm13.14}$	$6.92_{\pm0.30}$	$6.74_{\pm0.31}$
Back	$-348.67_{\pm7.93}$	$7.86_{\pm0.20}$	$7.36_{\pm0.21}$
Argon inlet	$-267.33_{\pm7.41}$	$0.48_{\pm0.02}$	$0.80_{\pm0.03}$

(b)

Figure 13 (a) Potentiodynamic polarisation curve of the samples in 3.5% w/v NaCl H_2O solution and (b) their respective corrosion potential, corrosion current density and corrosion rate. The uncertainty was estimated with a 95% confidence interval.

In order to gain insights regarding the interfacial characteristics of the passive film and on prevailing corrosion mechanisms, EIS measurements were performed. Figure 14a and Figure 14b show the EIS results depicted in the forms of Bode and Nyquist plots. The EIS data was further analysed using equivalent circuit modelling by fitting the data to a modified Randles circuit, Figure 14c. In this model, R_e is the uncompensated resistance of the electrolyte between the working and the reference electrode and R_{ct} represents the electrical resistance to the charge movement offered by the electrical double layer formed on the working electrode surface. A constant phase element (CPE) was used to represent the non-ideal capacitive behaviour of the electrical double layer forming at the working electrode-electrolyte interface [110]. The impedance of the constant phase element is defined as:

$$Z_{cpe} = \frac{1}{Y_0 (j\omega)^\alpha}$$

where j is the imaginary component ($j^2 = -1$) of the impedance, ω is the angular frequency ($2\pi f$) and Y_0 is the admittance of the CPE defined by the ease of alternating current flow into the circuit. The CPE represents an ideal capacitor behaviour when $\alpha = 1$ or intermediate characteristics between a capacitor and resistor when $0 < \alpha < 1$ [111,112]. The parameters of the equivalent electrical circuit obtained from simulation based on the EIS experimental data is shown in Figure 14d. In spite of the fact that the CPE element is related to the double layer capacitance, here, it does not behave as a pure capacitor since $\alpha < 1$. Therefore, in order to determine the effective double layer capacitance, the well-established Brug's equation was used [113], as expressed below:

$$C_{dl} = Y_0^{1/\alpha} (R_e^{-1} + R_{ct}^{-1})^{(\alpha-1)/\alpha}$$

According to the Bode plots of Figure 14a, the overall electrochemical behaviour of the samples follows the same trend and confirms the assumption of a single time constant, identified from the phase angle. At lower frequencies (i.e. <1 Hz), the polarisation resistance became dominant and these curves departed the higher frequency trend as they formed the low frequency plateau which represented the sum of R_e and R_{ct}. While at high frequencies (i.e. >10 kHz) the curve behaviour was related to R_e, which was much smaller than the charge transfer resistance, R_{ct}. At middle frequency ranges (i.e. 1 Hz to 10 kHz), the phase angle drop represents the capacitive response of the electric double layer and/or passive oxide film. In the low frequency region, there are apparent differences in the impedance modulus. These indicate that the samples exhibited dissimilar barrier properties of the oxide layer. Based on the phase angle, the argon inlet sample passive film is mainly capacitive, as an ideal capacitor has a phase angle of -90° [114]. A higher negative phase angle indicates an increase in the protective nature of the oxide film. The argon outlet peak phase angle shifted the most towards higher frequencies, which shows that the passive film became less stable, hence the risk of corrosion began to increase. The phase angle peak of the argon inlet is relatively flat (wider frequency range) in comparison to the other samples. This implies that its protective oxide layer remained intact over a longer period of time.

The EIS results presented as Nyquist plots are depicted in Figure 14b. The lowest Z_{real} value (high frequency) represented the R_e and the highest Z_{real} value represented the sum of R_e and R_{ct} at low frequencies. According to these plots, typical capacitive semicircles are similar for all samples, but with different radius. The larger the radius of the semicircle is indicative that the passive films formed by potentiodynamic polarisation present higher impedance response and that represents higher resistance to corrosion. As expected, the R_e was low and very similar for all samples. The argon outlet and back location samples showed significantly higher electrochemical reaction rates. This is clear from their lower R_{ct}, which is indicative of an enhanced charge transfer of chloride ions through the CPE and hence of a less protective film. The Y_0 values also justified the existence of a less uniform and defective oxide film on these samples. Therefore, the lower R_{ct} and larger Y_0 suggest the dissolution of oxides and formation of larger concentration of defect sites within the oxide films. It is important to notice the particularly higher R_{ct} of the argon inlet sample (233.25 Ωcm^2), which reflects to a higher stability of oxide film. This higher resistive behaviour could be directly related to its grain structure, lower grain boundary density and less surface defects (i.e. pores). In fact, in stainless steels, it is well-known that grain refinement is an important factor in passive film formation and growth [115–117]. Therefore, a refined grain structure could effectively decrease the diffusion path length for metal atoms to migrate toward the metal-electrolyte interface to form a protective and uniform passive film. In which, as a result, enables the thickening of the passive oxide film. According to the Helmholtz model and the standard expression for parallel plate capacitors, $L_{ss} = \varepsilon\varepsilon_0 A/C_{dl}$, the steady-state film thickness (L_{ss}) is inversely proportional to the C_{dl} [118,119]. Therefore, the C_{dl} results of Figure 14d help to explain the better corrosion performance of the argon inlet location sample.

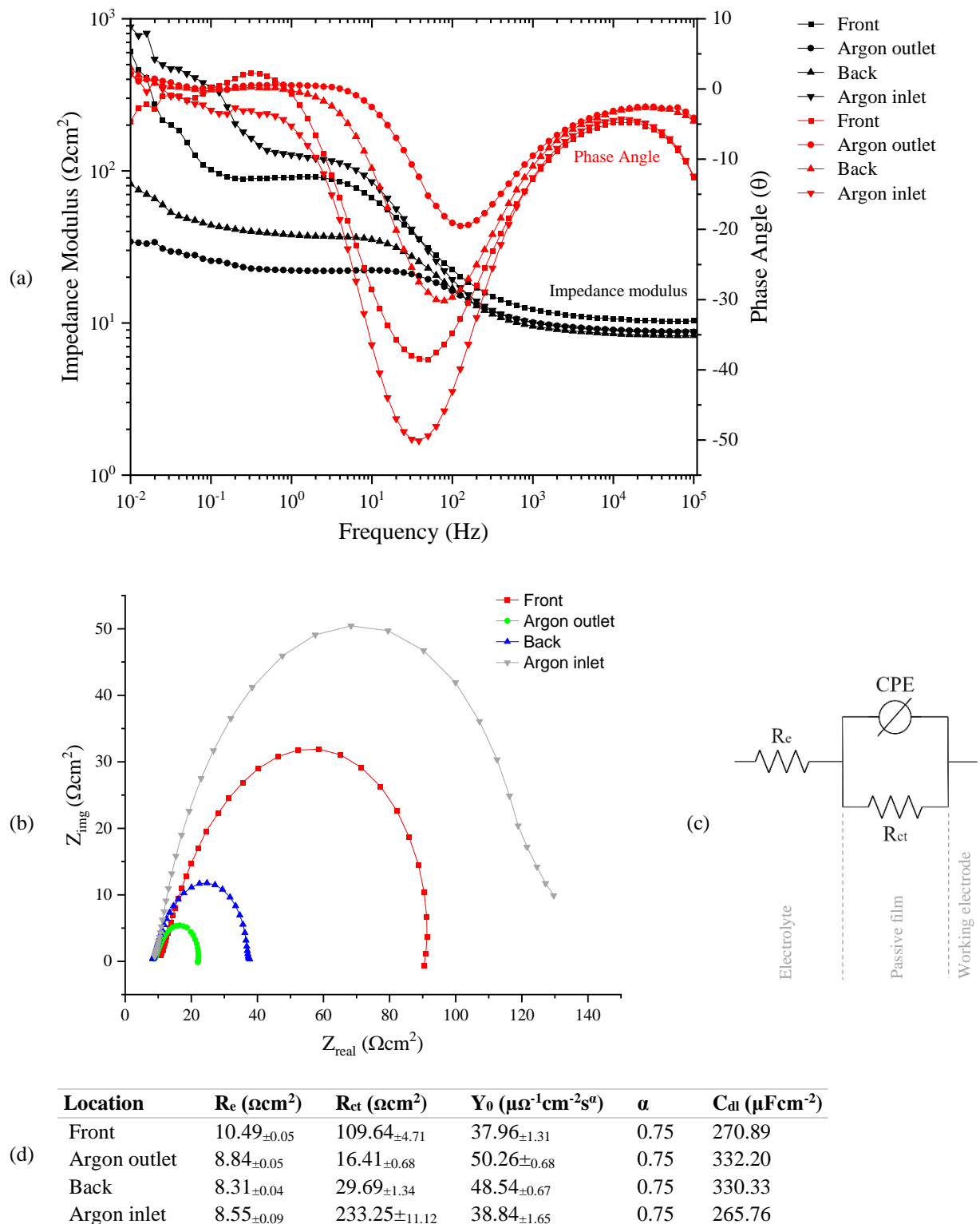| Location	R_e (Ωcm^2)	R_{ct} (Ωcm^2)	Y_0 ($\mu\Omega^{-1}cm^{-2}s^{\alpha}$)	α	C_{dl} (μFcm^{-2})
Front	$10.49_{\pm 0.05}$	$109.64_{\pm 4.71}$	$37.96_{\pm 1.31}$	0.75	270.89
Argon outlet	$8.84_{\pm 0.05}$	$16.41_{\pm 0.68}$	$50.26_{\pm 0.68}$	0.75	332.20
Back	$8.31_{\pm 0.04}$	$29.69_{\pm 1.34}$	$48.54_{\pm 0.67}$	0.75	330.33
Argon inlet	$8.55_{\pm 0.09}$	$233.25_{\pm 11.12}$	$38.84_{\pm 1.65}$	0.75	265.76

Figure 14 Electrochemical impedance spectroscopy data showing (a) the Bode plots and (b) the Nyquist plots recorded for the samples in 3.5% w/v NaCl H_2O solution; (c) the equivalent electrical circuit used to model the data and (d) the obtained equivalent electrical circuit parameters. The uncertainty was estimated with a 95% confidence interval.

3.2 Part Property Repeatability

3.2.1 Evidence of Repeatability Issues

The repeatability of the investigated properties based on the location parameter is shown in Figure 15. The calculation of the repeatability percentages was based on the classical analysis of coefficient of variation [120,121]. Each value was calculated for each specified sample property as calculated from three samples printed in different builds using the same location and sample production inputs. For easy visualisation of the effect of the location parameter, the repeatability percentages of each property is presented colour ranked from lowest to highest values. A large repeatability span for nanohardness and yield and ultimate tensile strengths was observed, implying that the location parameter had a considerable effect on the repeatability of these properties. On the contrary, the repeatability of density and Vickers hardness were less sensitive to the location parameter. It is clear from Figure 15 that none of the critical locations showed better all-around repeatability of the investigated properties. However, overall while having some lower levels of measured physical properties, the argon inlet location presented the best repeatability. The factors responsible for diminishing repeatability could be for example, unique processed-layer defects progressing and worsening through consecutive layers, inconsistent meltpool stabilities, temporal formation of inconsistent and multi-component non-homogeneous microstructures.

	Property	Part Location			
		Front	Argon outlet	Back	Argon inlet
	Density	98.84	98.55	98.96	98.88
	Vickers Hardness	99.46	99.57	99.44	99.31
Tensile Test	Modulus of Elasticity	97.96	97.69	96.28	97.02
	Tensile Strength, Yield	93.00	96.83	89.73	98.40
	Tensile Strength, Ultimate	95.46	87.83	91.72	97.43
Nanoindentation	Nanohardness	92.94	90.07	85.70	95.52
	Reduced Modulus	96.12	96.66	93.69	96.36
	Contact Stiffness	96.72	97.07	97.21	97.83
	Corrosion Rate	95.18	95.33	97.61	96.61

Ranking
Lowest [red][orange][blue][green] Highest

Figure 15 Part properties repeatability-dependency on printing location. The repeatability percentages of each property is colour ranked for easy visualisation of the effect of the location parameter.

To assess the significance of the properties variability induced by the location parameter, the probability values (p-values) were calculated. An α level of 0.01 was chosen to set limits of acceptable probability for the role of change in the measured distinctions. Then, statistical significance was proclaimed if the calculations yielded a p-value below α. Table 3 shows the summary of test statistics. From the investigated critical locations, statistical differences were identified in yield strength and hardness for samples printed near the argon inlet and argon outlet. An ideal argon condition for printing near the argon inlet location is less likely of efficiently preventing flying spatter powder from collapsing onto the meltpool and powder bed, and removing fumes and condensate at those parts being printed near argon outlet location. Additionally, the laminar argon flow exiting the argon inlet diffusor is likely to undergo a turbulent transition by the time it reaches the argon outlet location [122], as well as an obvious temperature increase as it flows over the hot build platform (powder bed), which is supported by a temperature difference observed between the argon inlet and argon outlet tubing at the argon filtration/cooling unit. Differently, an ideal argon condition for printing near the argon outlet location, which requires a higher argon velocity and flow rate, is typically observed blowing away powder from the powder bed near the argon inlet location. Therefore, it can be said that at the argon outlet and argon inlet printing locations, a slightly different processing condition exist for a given argon velocity and flow rate. As seen in Figure 15, a reasonable repeatability for the corrosion rate was achieved in all of the four critical locations. However, the variability of the corrosion rate between the locations was shown to be statistical significant in Table 3. In addition to the discussion in section 3.1.8, it is clear that the integrity, uniformity and morphology of the protective oxide film varies with the print

location parameter. One driving force for corrosion is the existence of heterogeneities in the material, ranging from atomic to several microns in scale, arising for example from crystal structure defects, segregation of elements and non-metallic inclusions [123,124]. Therefore, such factors could have contributed to corrosion activation and accelerated corrosion propagation. In conclusion, it can be said that the observed corrosion rate variability was related to the sample metallurgical characteristics developed by its location parameter.

Table 3 Test statistics summary showing the statistical significance of the properties variability based on the location which the sample was printed.

Property	P-value			
	Front	**Argon outlet**	**Back**	**Argon inlet**
Density	0.1373	0.0475	0.2298	0.1509
Vickers Hardness	0.4478	0.0053	0.3306	0.0138
Modulus of Elasticity	0.0494	0.0186	0.4923	0.1389
Tensile Strength, Yield	0.1581	0.0038	0.1949	0.0081
Tensile Strength, Ultimate	0.0566	0.0467	0.1626	0.0491
Nanohardness	0.0387	0.0877	0.1676	0.0065
Reduced Modulus	0.3867	0.1511	0.3645	0.0558
Contact Stiffness	0.0398	0.0644	0.0523	0.0502
Corrosion Rate	0.0013	0.0004	0.0003	0.0001

Hypothesis	Significance level $\alpha = 0.01$	Colour code
$H_0: \mu = \overline{x}$	$P - value \ < \ \alpha \ \rightarrow \ reject \ H_0$	$P - value \ < \ 0.01$
$H_a: \mu \neq \overline{x}$	$P - value \geq \alpha \ \rightarrow \ fail \ to \ reject \ H_0$	$P - value \ \geq \ 0.01$

3.2.2 Attributes Impairing Repeatability

Unfortunately, different definitions for repeatability in published work related to additive manufacturing are still used [125–128,121,129–131]. Repeatability is also sometimes wrongly addressed as replicability (printed in the same or different site, different operator, same experimental setup, different builds) and reproducibility (printed in different site, different operator, different experimental setup, different builds) [132–134]. One of the reasons could be the fact that additive manufacturing technologies are adopted by different scientific disciplines and institutions. As a consequence, each of them may prefer to apply their own definitions and hence introduce confusion to the definition of these terminologies [135]. Recently, the American Society for Testing Materials (ASTM) developed a number of additive manufacturing standards intended to help the implementation of additive manufacturing technologies [136]. Including the ASTM 52900 standard which defines repeatability as the degree of measurable properties between identical parts, printed by the same operator, using the same printer and input parameters, but printed in different builds [137]. At present, there is no certified guideline on how to report property variability between parts printed in the same build. In order to efficiently tackle the repeatability issue in additive manufacturing, the aforementioned issues should be addressed first.

In modern L-PBF processing, between 150 and 200 input parameters exist and have an influence on the ultimate quality of printed components. The total number of input parameters varies depending mainly on the feedstock material (i.e. form and quantity), printing file (number of commands and amount of layer detail) and printer (i.e. model and capability). Since the underlying source of repeatability issues is unclear, it is imperative to look beyond the commonly studied input parameters and focus more on other less or not yet studied input parameters. In-situ real-time monitoring and closed-loop process control should be implemented and used to improve repeatability. Until then, repeatability will continue to be an issue for L-PBF which needs to be well measured and recorded in

relation to the process input parameters. As a reference, an acceptable repeatability is the one that fulfils the minimum requirements to serve practical purposes for each specific industry part requirement.

4. Conclusions

The present study provides a comprehensive insight into the effect of the part location parameter on the properties of components manufactured using L-PBF. The isolation of location from the other input parameters enabled an accurate quantification of part property variability caused by this parameter. In total, four critical locations on a build platform were examined, here named as front, argon outlet, back and argon inlet, which are locations prone variability in part properties. Hence, these locations were considered to assess the extent of this phenomenon.

Based on this study, the main conclusions are summarised below:

(1) A statistical difference in the part properties was found depending on the location where the part was printed. Therefore, an effect of the printing location on resultant part properties exists and should be considered depending on produced part application requirements.

(2) The repeatability (build-to-build) was found to vary across locations. This was because some of the locations were more susceptible to meltpool instabilities and spatter. The reduction in part-property repeatability was due to variation in microstructure and defects for the same location in successive builds.

(3) The front location promoted enhanced part densification due to a higher powder bed packing resultant from the inevitable particle segregation phenomenon taking place during powder spreading and due to a reduced volume of pores and voids within the part bulk microstructure.

(4) Parts printed near the argon outlet were more liable to internal defects. Nevertheless, superior hardness was measured from the argon outlet parts and related to their crystal orientation and grain size.

(5) Similar tensile performance was obtained for the parts printed at the front, back and argon inlet locations. The poor elongation to failure and inferior tensile strength of the argon outlet parts were ascribed to porosity and lack of fusion defects at this location. Banded grains present in the microstructure of the parts printed in the front location contributed to ductility, while the higher and constant strain hardening rate of these parts was accredited to a stronger crystallographic texture which promoted a longer twinning period and higher twin density.

(6) The influence of the location parameter on the corrosion behaviour of parts was evidenced by the electrochemical measurements. In fact, parts printed at the argon outlet and back locations showed substantially higher electrochemical reactions, dissolution of oxides and formation of defect sites within the oxide films. In contrast, the argon inlet parts formed a much more stable and thicker protective film which remained intact over a longer period of time. The superior corrosion resistance evidenced by the determined lower corrosion rate of the argon inlet parts were attributed to their lower level of porosity and their small grain structures.

Acknowledgments

Supplementary Data

The following is supplementary material to this article.

References

[1] Kotadia, H. R., Gibbons, G., Das, A., and Howes, P. D., 2021, "A Review of Laser Powder Bed Fusion Additive Manufacturing of Aluminium Alloys: Microstructure and Properties," Addit. Manuf., **46**.

[2] Tofail, S. A. M., Koumoulos, E. P., Bandyopadhyay, A., Bose, S., O'Donoghue, L., and Charitidis, C., 2018, "Additive Manufacturing: Scientific and Technological Challenges, Market Uptake and Opportunities," Mater. Today, **21**(1), pp. 22–37.

[3] Mussatto, A., Ahad, I. U., Mousavian, R. T., Delaure, Y., and Brabazon, D., 2020, "Advanced Production Routes for Metal Matrix Composites," Eng. Rep., pp. 1–25.

[4] Thomas-Seale, L. E. J., Kirkman-Brown, J. C., Attallah, M. M., Espino, D. M., and Shepherd, D. E. T., 2018, "The Barriers to the Progression of Additive Manufacture: Perspectives from UK Industry," Int. J. Prod. Econ., **198**, pp. 104–118.

[5] Liu, C., Le Roux, L., Körner, C., Tabaste, O., Lacan, F., and Bigot, S., 2020, "Digital Twin-Enabled Collaborative Data Management for Metal Additive Manufacturing Systems," J. Manuf. Syst.

[6] Schmidt, M., Merklein, M., Bourell, D., Dimitrov, D., Hausotte, T., Wegener, K., Overmeyer, L., Vollertsen, F., and Levy, G. N., 2017, "Laser Based Additive Manufacturing in Industry and Academia," CIRP Ann., **66**(2), pp. 561–583.

[7] Spears, T. G., and Gold, S. A., 2016, "In-Process Sensing in Selective Laser Melting (SLM) Additive Manufacturing," Integrating Mater. Manuf. Innov., **5**(1), pp. 16–40.

[8] Dowling, L., Kennedy, J., O'Shaughnessy, S., and Trimble, D., 2020, "A Review of Critical Repeatability and Reproducibility Issues in Powder Bed Fusion," Mater. Des., **186**, p. 108346.

[9] Oliveira, J. P., LaLonde, A. D., and Ma, J., 2020, "Processing Parameters in Laser Powder Bed Fusion Metal Additive Manufacturing," Mater. Des., **193**(108762).

[10] ISO/ASTM52921, 2019, *Standard Terminology for Additive Manufacturing - Coordinate Systems and Test Methodologies*, ASTM International, West Conshohocken, PA.

[11] Karimi, P., Sadeghi, E., Ålgårdh, J., Harlin, P., and Andersson, J., 2020, "Effect of Build Location on Microstructural Characteristics and Corrosion Behavior of EB-PBF Built Alloy 718," Int. J. Adv. Manuf. Technol., **106**(7), pp. 3597–3607.

[12] Calignano, F., 2018, "Investigation of the Accuracy and Roughness in the Laser Powder Bed Fusion Process," Virtual Phys. Prototyp., **13**(2), pp. 97–104.

[13] Hitzler, L., Hirsch, J., Merkel, M., Hall, W., and Öchsner, A., 2017, "Position Dependent Surface Quality in Selective Laser Melting," Mater. Werkst., **48**(5), pp. 327–334.

[14] Mertová, K., Džugan, J., Roudnická, M., Daniel, M., Vojtěch, D., Seifi, M., and Lewandowski, J. J., 2020, "Build Size and Orientation Influence on Mechanical Properties of Powder Bed Fusion Deposited Titanium Parts," Metals, **10**(10), p. 1340.

[15] Croccolo, D., Agostinis, M. D., Fini, S., Olmi, G., Bogojevic, N., and Ciric-Kostic, S., 2018, "Effects of Build Orientation and Thickness of Allowance on the Fatigue Behaviour of 15–5 PH Stainless Steel Manufactured by DMLS," Fatigue Fract. Eng. Mater. Struct., **41**(4), pp. 900–916.

[16] Shen, H., Rometsch, P., Wu, X., and Huang, A., 2020, "Influence of Gas Flow Speed on Laser Plume Attenuation and Powder Bed Particle Pickup in Laser Powder Bed Fusion," JOM, **72**(3), pp. 1039–1051.

[17] Ahmed Obeidi, M., Mussatto, A., Groarke, R., Vijayaraghavan, R. K., Conway, A., Rossi Kaschel, F., McCarthy, E., Clarkin, O., O'Connor, R., and Brabazon, D., 2020, "Comprehensive Assessment of Spatter Material Generated during Selective Laser Melting of Stainless Steel," Mater. Today Commun., **25**, p. 101294.

[18] Chua, G. K. H., Choong, Y. Y. C., and Wong, C. H., 2018, "Investigation of the Effects on the Print Location during Selective Laser Melting Process," *Proceedings of the 3rd International Conference on Progress in Additive Manufacturing*, Pro-AM Conference Papers, Singapore, pp. 613–618.

[19] Hrabe, N., and Quinn, T., 2013, "Effects of Processing on Microstructure and Mechanical Properties of a Titanium Alloy (Ti–6Al–4V) Fabricated Using Electron Beam Melting (EBM), Part 2: Energy Input, Orientation, and Location," Mater. Sci. Eng. A, **573**, pp. 271–277.

[20] Re, F. D., Scherillo, F., Contaldi, V., Palumbo, B., Squillace, A., Corrado, P., and Petta, P. D., 2019, "Mechanical Properties Characterisation of AlSi10Mg Parts Produced by Laser Powder Bed Fusion Additive Manufacturing," Int. J. Mater. Res., **110**(5), pp. 436–446.

[21] Seifi, M., Dahar, M., Aman, R., Harrysson, O., Beuth, J., and Lewandowski, J. J., 2015, "Evaluation of Orientation Dependence of Fracture Toughness and Fatigue Crack Propagation Behavior of As-Deposited ARCAM EBM Ti-6Al-4V," JOM, **67**(3), pp. 597–607.

[22] Drexler, M., Lexow, M., and Drummer, D., 2015, "Selective Laser Melting of Polymer Powder - Part Mechanics as Function of Exposure Speed," Phys. Procedia, **78**, pp. 328–336.

[23] Grasso, M., and Colosimo, B. M., 2017, "Process Defects and in Situ Monitoring Methods in Metal Powder Bed Fusion: A Review," Meas. Sci. Technol., **28**(4), pp. 1–25.

[24] Moorthy, S., 2017, "Modeling and Characterization of Mechanical Properties in Laser Powder Bed Fusion Additive Manufactured Inconel 718," Masters theses, Colorado School of Mines.

[25] Soltani-Tehrani, A., Pegues, J., and Shamsaei, N., 2020, "Fatigue Behavior of Additively Manufactured 17-4 PH Stainless Steel: The Effects of Part Location and Powder Re-Use," Addit. Manuf., **36**, p. 101398.

[26] Mussatto, A., Groarke, R., O'Neill, A., Obeidi, M. A., Delaure, Y., and Brabazon, D., 2021, "Influences of Powder Morphology and Spreading Parameters on the Powder Bed Topography Uniformity in Powder Bed Fusion Metal Additive Manufacturing," Addit. Manuf., **38**, p. 101807.

[27] Cordova, L., Bor, T., de Smit, M., Campos, M., and Tinga, T., 2020, "Measuring the Spreadability of Pre-Treated and Moisturized Powders for Laser Powder Bed Fusion," Addit. Manuf., **32**, p. 101082.

[28] Gibson, B. T., and Lowden, R. A., 2018, *Process Development for Selective Laser Melting of Molybdenum*, ORNL/SPR-2018/1045, Oak Ridge National Laboratory, United States.

[29] Alfaify, A., 2019, "The Effect of Changing Particle Size Distribution and Layer Thickness on the Density of Parts Manufactured Using the Laser Powder Bed Fusion Process," PhD thesis, University of Sheffield.

[30] ASTM E8/E8M, 2009, *Standard Test Methods for Tension Testing of Metallic Materials*, ASTM International, West Conshohocken, PA.

[31] ASTM B962, 2017, *Standard Test Methods for Density of Compacted or Sintered Powder Metallurgy (PM) Products Using Archimedes' Principle*, ASTM International, West Conshohocken, PA.

[32] ASTM E92, 2017, *Standard Test Methods for Vickers Hardness and Knoop Hardness of Metallic Materials*, West Conshohocken, PA.

[33] Zhang, B., Li, Y., and Bai, Q., 2017, "Defect Formation Mechanisms in Selective Laser Melting: A Review," Chin. J. Mech. Eng., **30**(3), pp. 515–527.

[34] Louvis, E., Fox, P., and Sutcliffe, C. J., 2011, "Selective Laser Melting of Aluminium Components," J. Mater. Process. Technol., **211**(2), pp. 275–284.

[35] Das, S., 2003, "Physical Aspects of Process Control in Selective Laser Sintering of Metals," Adv. Eng. Mater., **5**(10), pp. 701–711.

[36] Vilaro, T., Colin, C., and Bartout, J. D., 2011, "As-Fabricated and Heat-Treated Microstructures of the Ti-6Al-4V Alloy Processed by Selective Laser Melting," Metall. Mater. Trans. A, **42**(10), pp. 3190–3199.

[37] de Terris, T., Andreau, O., Peyre, P., Adamski, F., Koutiri, I., Gorny, C., and Dupuy, C., 2019, "Optimization and Comparison of Porosity Rate Measurement Methods of Selective Laser Melted Metallic Parts," Addit. Manuf., **28**, pp. 802–813.

[38] Yadroitsev, I., Gusarov, A., Yadroitsava, I., and Smurov, I., 2010, "Single Track Formation in Selective Laser Melting of Metal Powders," J. Mater. Process. Technol., **210**(12), pp. 1624–1631.

[39] DebRoy, T., Wei, H. L., Zuback, J. S., Mukherjee, T., Elmer, J. W., Milewski, J. O., Beese, A. M., Wilson-Heid, A., De, A., and Zhang, W., 2018, "Additive Manufacturing of Metallic Components – Process, Structure and Properties," Prog. Mater. Sci., **92**, pp. 112–224.

[40] Gunenthiram, V., Peyre, P., Schneider, M., Dal, M., Coste, F., and Fabbro, R., 2017, "Analysis of Laser–Melt Pool–Powder Bed Interaction during the Selective Laser Melting of a Stainless Steel," J. Laser Appl., **29**(2), p. 022303.

[41] Reijonen, J., Revuelta, A., Riipinen, T., Ruusuvuori, K., and Puukko, P., 2020, "On the Effect of Shielding Gas Flow on Porosity and Melt Pool Geometry in Laser Powder Bed Fusion Additive Manufacturing," Addit. Manuf., **32**.

[42] Marattukalam, J. J., Karlsson, D., Pacheco, V., Beran, P., Wiklund, U., Jansson, U., Hjörvarsson, B., and Sahlberg, M., 2020, "The Effect of Laser Scanning Strategies on Texture, Mechanical Properties, and Site-Specific Grain Orientation in Selective Laser Melted 316L SS," Mater. Des., **193**, p. 108852.

[43] Liu, Y., Pang, Z., and Zhang, J., 2017, "Comparative Study on the Influence of Subsequent Thermal Cycling on Microstructure and Mechanical Properties of Selective Laser Melted 316L Stainless Steel," Appl. Phys. A, **123**(11), p. 688.

[44] Laleh, M., Hughes, A. E., Xu, W., Haghdadi, N., Wang, K., Cizek, P., Gibson, I., and Tan, M. Y., 2019, "On the Unusual Intergranular Corrosion Resistance of 316L Stainless Steel Additively Manufactured by Selective Laser Melting," Corros. Sci., **161**, p. 108189.

[45] Rowe, L. C., 1977, "The Application of Corrosion Principles to Engineering Design," SAE Trans., **86**, pp. 1379–1392.

[46] Virtanen, S., Schmuki, P., and Frankel, G. S., 2003, "Intergranular Corrosion Morphology and Growth Kinetics in High Strength Aluminium Alloys," *Critical Factors in Localized Corrosion IV: A Symposium in Honor of the 65th Birthday of Hans Böhni : Proceedings of the International Symposium*, The Electrochemical Society, Salt Lake City, United States, pp. 159–167.

[47] Ball, P., 2008, "Steel Toughened by Pancakes: New Treatment Set to Improve Steel's Properties at Low Cost," Nature, p. news.2008.851.

[48] Bahl, S., Mishra, S., Yazar, K. U., Kola, I. R., Chatterjee, K., and Suwas, S., 2019, "Non-Equilibrium Microstructure, Crystallographic Texture and Morphological Texture Synergistically Result in Unusual Mechanical Properties of 3D Printed 316L Stainless Steel," Addit. Manuf., **28**, pp. 65–77.

[49] Ahmed Obeidi, M., Uí Mhurchadha, S. M., Raghavendra, R., Conway, A., Souto, C., Tormey, D., Ahad, I. U., and Brabazon, D., 2021, "Comparison of the Porosity and Mechanical Performance of 316L Stainless Steel Manufactured on Different Laser Powder Bed Fusion Metal Additive Manufacturing Machines," J. Mater. Res. Technol., **13**, pp. 2361–2374.

[50] Wang, Y. M., Voisin, T., McKeown, J. T., Ye, J., Calta, N. P., Li, Z., Zeng, Z., Zhang, Y., Chen, W., Roehling, T. T., Ott, R. T., Santala, M. K., Depond, P. J., Matthews, M. J., Hamza, A. V., and Zhu, T., 2018, "Additively Manufactured Hierarchical Stainless Steels with High Strength and Ductility," Nat. Mater., **17**(1), pp. 63–71.

[51] Gallmeyer, T. G., Moorthy, S., Kappes, B. B., Mills, M. J., Amin-Ahmadi, B., and Stebner, A. P., 2020, "Knowledge of Process-Structure-Property Relationships to Engineer Better Heat Treatments for Laser Powder Bed Fusion Additive Manufactured Inconel 718," Addit. Manuf., **31**.

[52] Liu, L., Ding, Q., Zhong, Y., Zou, J., Wu, J., Chiu, Y.-L., Li, J., Zhang, Z., Yu, Q., and Shen, Z., 2018, "Dislocation Network in Additive Manufactured Steel Breaks Strength–Ductility Trade-Off," Mater. Today, **21**(4), pp. 354–361.

[53] Wang, X., Muñiz-Lerma, J. A., Sánchez-Mata, O., Attarian Shandiz, M., and Brochu, M., 2018, "Microstructure and Mechanical Properties of Stainless Steel 316L Vertical Struts Manufactured by Laser Powder Bed Fusion Process," Mater. Sci. Eng. A, **736**, pp. 27–40.

[54] Röttger, A., Boes, J., Theisen, W., Thiele, M., Esen, C., Edelmann, A., and Hellmann, R., 2020, "Microstructure and Mechanical Properties of 316L Austenitic Stainless Steel Processed by Different SLM Devices," Int. J. Adv. Manuf. Technol., **108**(3), pp. 769–783.

[55] Kempf, A., and Hilgenberg, K., 2020, "Influence of Sub-Cell Structure on the Mechanical Properties of AlSi10Mg Manufactured by Laser Powder Bed Fusion," Mater. Sci. Eng. A, **776**.

[56] Cui, L., Jiang, F., Deng, D., Xin, T., Sun, X., Mousavian, R. T., Peng, R. L., Yang, Z., and Moverare, J., 2021, "Cyclic Response of Additive Manufactured 316L Stainless Steel: The Role of Cell Structures," Scr. Mater., **205**.

[57] Callister, W., and Rethwisch, D. G., 2018, *Fundamentals of Materials Science and Engineering: An Integrated Approach*, John Wiley & Sons, New Jersey.

[58] Eschner, N., Weiser, L., Häfner, B., and Lanza, G., 2020, "Classification of Specimen Density in Laser Powder Bed Fusion (L-PBF) Using in-Process Structure-Borne Acoustic Process Emissions," Addit. Manuf., **34**, p. 101324.

[59] Pal, S., Lojen, G., Kokol, V., and Drstvenšek, I., 2019, "Reducing Porosity at the Starting Layers above Supporting Bars of the Parts Made by Selective Laser Melting," Powder Technol., **355**, pp. 268–277.

[60] Nath, S. D., Irrinki, H., Gupta, G., Kearns, M., Gulsoy, O., and Atre, S., 2019, "Microstructure-Property Relationships of 420 Stainless Steel Fabricated by Laser-Powder Bed Fusion," Powder Technol., **343**, pp. 738–746.

[61] Bai, Y., Wagner, G., and Williams, C. B., 2017, "Effect of Particle Size Distribution on Powder Packing and Sintering in Binder Jetting Additive Manufacturing of Metals," J. Manuf. Sci. Eng., **139**(8).

[62] Mindt, H. W., Megahed, M., Lavery, N. P., Holmes, M. A., and Brown, S. G. R., 2016, "Powder Bed Layer Characteristics: The Overseen First-Order Process Input," Metall. Mater. Trans. A, **47**(8), pp. 3811–3822.

[63] Mao, K. S., Sun, C., Huang, Y., Shiau, C.-H., Garner, F. A., Freyer, P. D., and Wharry, J. P., 2019, "Grain Orientation Dependence of Nanoindentation and Deformation-Induced Martensitic Phase Transformation in Neutron Irradiated AISI 304L Stainless Steel," Materialia, **5**, p. 100208.

[64] Fischer-Cripps, A. C., 2006, "Critical Review of Analysis and Interpretation of Nanoindentation Test Data," Surf. Coat. Technol., **200**(14), pp. 4153–4165.

[65] Broitman, E., 2016, "Indentation Hardness Measurements at Macro-, Micro-, and Nanoscale: A Critical Overview," Tribol. Lett., **65**(1), p. 23.

[66] Yakout, M., Elbestawi, M. A., and Veldhuis, S. C., 2019, "Density and Mechanical Properties in Selective Laser Melting of Invar 36 and Stainless Steel 316L," J. Mater. Process. Technol., **266**, pp. 397–420.

[67] Musil, J., Kunc, F., Zeman, H., and Poláková, H., 2002, "Relationships between Hardness, Young's Modulus and Elastic Recovery in Hard Nanocomposite Coatings," Surf. Coat. Technol., **154**(2), pp. 304–313.

[68] Briscoe, B. J., Fiori, L., and Pelillo, E., 1998, "Nano-Indentation of Polymeric Surfaces," J. Phys. Appl. Phys., **31**(19), pp. 2395–2405.

[69] Nasim, M., Li, Y., and Wen, C., 2021, "Individual Layer Thickness-Dependent Nanoindentation and Nanotribological Behaviors of Ta/Co Nanolaminates," Tribol. Int., **156**, p. 106845.

[70] Hynowska, A., Pellicer, E., Fornell, J., González, S., van Steenberge, N., Suriñach, S., Gebert, A., Calin, M., Eckert, J., Baró, M. D., and Sort, J., 2012, "Nanostructured β-Phase Ti–31.0Fe–9.0Sn and Sub-Mm

Structured Ti–39.3Nb–13.3Zr–10.7Ta Alloys for Biomedical Applications: Microstructure Benefits on the Mechanical and Corrosion Performances," Mater. Sci. Eng. C, **32**(8), pp. 2418–2425.

[71] Tiamiyu, A. A., Tari, V., Szpunar, J. A., Odeshi, A. G., and Khan, A. K., 2018, "Effects of Grain Refinement on the Quasi-Static Compressive Behavior of AISI 321 Austenitic Stainless Steel: EBSD, TEM, and XRD Studies," Int. J. Plast., **107**, pp. 79–99.

[72] Tiamiyu, A. A., Odeshi, A. G., and Szpunar, J. A., 2018, "Multiple Strengthening Sources and Adiabatic Shear Banding during High Strain-Rate Deformation of AISI 321 Austenitic Stainless Steel: Effects of Grain Size and Strain Rate," Mater. Sci. Eng. A, **711**, pp. 233–249.

[73] Ghanbari, S., and Bahr, D. F., 2019, "An Energy-Based Nanoindentation Method to Assess Localized Residual Stresses and Mechanical Properties on Shot-Peened Materials," J. Mater. Res., **34**(7), pp. 1121–1129.

[74] Lee, J., Lee, C., and Kim, B., 2009, "Reverse Analysis of Nano-Indentation Using Different Representative Strains and Residual Indentation Profiles," Mater. Des., **30**(9), pp. 3395–3404.

[75] Yan, F. K., Liu, G. Z., Tao, N. R., and Lu, K., 2012, "Strength and Ductility of 316L Austenitic Stainless Steel Strengthened by Nano-Scale Twin Bundles," Acta Mater., **60**(3), pp. 1059–1071.

[76] Calcagnotto, M., Ponge, D., and Raabe, D., 2010, "Effect of Grain Refinement to 1μm on Strength and Toughness of Dual-Phase Steels," Mater. Sci. Eng. A, **527**(29), pp. 7832–7840.

[77] Bartolomeu, F., Buciumeanu, M., Pinto, E., Alves, N., Carvalho, O., Silva, F. S., and Miranda, G., 2017, "316L Stainless Steel Mechanical and Tribological Behavior—A Comparison between Selective Laser Melting, Hot Pressing and Conventional Casting," Addit. Manuf., **16**, pp. 81–89.

[78] Wang, Y. M., Voisin, T., McKeown, J. T., Ye, J., Calta, N. P., Li, Z., Zeng, Z., Zhang, Y., Chen, W., Roehling, T. T., Ott, R. T., Santala, M. K., Depond, P. J., Matthews, M. J., Hamza, A. V., and Zhu, T., 2018, "Additively Manufactured Hierarchical Stainless Steels with High Strength and Ductility," Nat. Mater., **17**(1), pp. 63–71.

[79] Anwar, A. B., and Pham, Q.-C., 2017, "Selective Laser Melting of AlSi10Mg: Effects of Scan Direction, Part Placement and Inert Gas Flow Velocity on Tensile Strength," J. Mater. Process. Technol., **240**, pp. 388–396.

[80] Rollett, A. D., and Kocks, U. F., 1993, *A Review of the Stages of Work Hardening*, LA-UR-93-2339; CONF-9304166-1, Los Alamos National Lab, New Mexico.

[81] Kurz, W., and Fisher, D. J., 1998, *Fundamentals of Solidification*, Trans Tech Publications Ltd, Zurich, Switzerland.

[82] Kocks, U. F., and Mecking, H., 2003, "Physics and Phenomenology of Strain Hardening: The FCC Case," Prog. Mater. Sci., **48**(3), pp. 171–273.

[83] Zehetbauer, M., and Seumer, V., 1993, "Cold Work Hardening in Stages IV and V of F.C.C. Metals—I. Experiments and Interpretation," Acta Metall. Mater., **41**(2), pp. 577–588.

[84] El-Danaf, E., Kalidindi, S. R., Doherty, R. D., and Necker, C., 2000, "Deformation Texture Transition in Brass: Critical Role of Micro-Scale Shear Bands," Acta Mater., **48**(10), pp. 2665–2673.

[85] Wenk, H. R., 1985, *Preferred Orientation in Deformed Metal and Rocks: An Introduction to Modern Texture Analysis*, Academic Press Inc., California.

[86] Mussatto, A., Groarke, R., A-Hameed, A., Ahad, I. U. I., Vijayaraghavan, R. K., O'Neill, A., McNally, P., Delaure, Y., and Brabazon, D., 2019, "Evaluation via Powder Metallurgy of Nano-Reinforced Iron Powders Developed for Selective Laser Melting Applications," Mater. Des., **182**, p. 108046.

[87] Sun, Z., Tan, X., Tor, S. B., and Chua, C. K., 2018, "Simultaneously Enhanced Strength and Ductility for 3D-Printed Stainless Steel 316L by Selective Laser Melting," NPG Asia Mater., **10**(4), pp. 127–136.

[88] Khorsand Zak, A., Abd. Majid, W. H., Abrishami, M. E., and Yousefi, R., 2011, "X-Ray Analysis of ZnO Nanoparticles by Williamson–Hall and Size–Strain Plot Methods," Solid State Sci., **13**(1), pp. 251–256.

[89] Fultz, B., and Howe, J. M., 2012, *Transmission Electron Microscopy and Diffractometry of Materials*, Springer Science & Business Media, Heidelberg.

[90] Humphreys, F. J., and Hatherly, M., 1995, *Recrystallization and Related Annealing Phenomena*, Elsevier Science Ltd, Oxford.

[91] Mola, J., 2017, "Considerations in the Design of Formable Austenitic Stainless Steels Based on Deformation-Induced Processes," *Austenitic Stainless Steels - New Aspects*, IntechOpen, Croatia, pp. 7–28.

[92] Woo, W., Naeem, M., Jeong, J.-S., Lee, C.-M., Harjo, S., Kawasaki, T., He, H., and Wang, X.-L., 2020, "Comparison of Dislocation Density, Twin Fault Probability, and Stacking Fault Energy between CrCoNi and CrCoNiFe Medium Entropy Alloys Deformed at 293 and 140K," Mater. Sci. Eng. A, **781**, p. 139224.

[93] Schramm, R. E., and Reed, R. P., 1975, "Stacking Fault Energies of Seven Commercial Austenitic Stainless Steels," Metall. Trans. A, **6**(7), p. 1345.

[94] Teklu, A., Ledbetter, H., Kim, S., Boatner, L. A., McGuire, M., and Keppens, V., 2004, "Single-Crystal Elastic Constants of Fe-15Ni-15Cr Alloy," Metall. Mater. Trans. A, **35**(10), pp. 3149–3154.

[95] Wu, X. X., San, X. Y., Liang, X. G., Gong, Y. L., and Zhu, X. K., 2013, "Effect of Stacking Fault Energy on Mechanical Behavior of Cold-Forging Cu and Cu Alloys," Mater. Des., **47**, pp. 372–376.

[96] Branicio, P. S., Zhang, J. Y., and Srolovitz, D. J., 2013, "Effect of Strain on the Stacking Fault Energy of Copper: A First-Principles Study," Phys. Rev. B, **88**(6), p. 064104.

[97] Achmad, T. L., Fu, W., Chen, H., Zhang, C., and Yang, Z.-G., 2018, "Effect of Strain on the Intrinsic Stacking Fault Energy of Fcc Co: A First-Principles Study," J. Mater. Sci., **53**(14), pp. 10217–10230.

[98] Dovgyy, B., Piglione, A., Hooper, P. A., and Pham, M.-S., 2020, "Comprehensive Assessment of the Printability of CoNiCrFeMn in Laser Powder Bed Fusion," Mater. Des., **194**.

[99] Wan, H. Y., Zhou, Z. J., Li, C. P., Chen, G. F., and Zhang, G. P., 2018, "Effect of Scanning Strategy on Grain Structure and Crystallographic Texture of Inconel 718 Processed by Selective Laser Melting," J. Mater. Sci. Technol., **34**(10), pp. 1799–1804.

[100] Chen, L., Richter, B., Zhang, X., Bertsch, K. B., Thoma, D. J., and Pfefferkorn, F. E., 2021, "Effect of Laser Polishing on the Microstructure and Mechanical Properties of Stainless Steel 316L Fabricated by Laser Powder Bed Fusion," Mater. Sci. Eng. A, **802**.

[101] Riabov, D., Leicht, A., Ahlström, J., and Hryha, E., 2021, "Investigation of the Strengthening Mechanism in 316L Stainless Steel Produced with Laser Powder Bed Fusion," Mater. Sci. Eng. A, **822**.

[102] Voisin, T., Forien, J.-B., Perron, A., Aubry, S., Bertin, N., Samanta, A., Baker, A., and Wang, Y. M., 2021, "New Insights on Cellular Structures Strengthening Mechanisms and Thermal Stability of an Austenitic Stainless Steel Fabricated by Laser Powder-Bed-Fusion," Acta Mater., **203**.

[103] Hong, Y., Zhou, C., Zheng, Y., Zhang, L., and Zheng, J., 2021, "The Cellular Boundary with High Density of Dislocations Governed the Strengthening Mechanism in Selective Laser Melted 316L Stainless Steel," Mater. Sci. Eng. A, **799**.

[104] Donik, Č., Kraner, J., Paulin, I., and Godec, M., 2020, "Influence of the Energy Density for Selective Laser Melting on the Microstructure and Mechanical Properties of Stainless Steel," Metals, **10**(7).

[105] Leicht, A., Rashidi, M., Klement, U., and Hryha, E., 2020, "Effect of Process Parameters on the Microstructure, Tensile Strength and Productivity of 316L Parts Produced by Laser Powder Bed Fusion," Mater. Charact., **159**.

[106] Jaskari, M., Ghosh, S., Miettunen, I., Karjalainen, P., and Järvenpää, A., 2021, "Tensile Properties and Deformation of AISI 316L Additively Manufactured with Various Energy Densities," Materials, **14**(19).

[107] Stansbury, E. E., and Buchanan, R. A., 2000, *Fundamentals of Electrochemical Corrosion*, ASM International, Ohio.

[108] ASTM G102-89, 2015, *Practice for Calculation of Corrosion Rates and Related Information from Electrochemical Measurements*, ASTM International, West Conshohocken, PA.

[109] Milošev, I., and Strehblow, H.-H., 2000, "The Behavior of Stainless Steels in Physiological Solution Containing Complexing Agent Studied by X-Ray Photoelectron Spectroscopy," J. Biomed. Mater. Res., **52**(2), pp. 404–412.

[110] Chen, H., Zhang, C., Jia, D., Wellmann, D., and Liu, W., 2020, "Corrosion Behaviors of Selective Laser Melted Aluminum Alloys: A Review," Metals, **10**(1), p. 102.

[111] Yuan, X.-Z. (Riny), Song, C., Wang, H., and Zhang, J., 2009, *Electrochemical Impedance Spectroscopy in PEM Fuel Cells: Fundamentals and Applications*, Springer Science & Business Media.

[112] Lvovich, V. F., 2012, *Impedance Spectroscopy: Applications to Electrochemical and Dielectric Phenomena*, John Wiley & Sons.

[113] Brug, G. J., van den Eeden, A. L. G., Sluyters-Rehbach, M., and Sluyters, J. H., 1984, "The Analysis of Electrode Impedances Complicated by the Presence of a Constant Phase Element," J. Electroanal. Chem. Interfacial Electrochem., **176**(1), pp. 275–295.

[114] Orazem, M. E., and Tribollet, B., 2011, *Electrochemical Impedance Spectroscopy*, John Wiley & Sons.

[115] Lodhi, M. J. K., Deen, K. M., Greenlee-Wacker, M. C., and Haider, W., 2019, "Additively Manufactured 316L Stainless Steel with Improved Corrosion Resistance and Biological Response for Biomedical Applications," Addit. Manuf., **27**, pp. 8–19.

[116] Balusamy, T., Kumar, S., and Sankara Narayanan, T. S. N., 2010, "Effect of Surface Nanocrystallization on the Corrosion Behaviour of AISI 409 Stainless Steel," Corros. Sci., **52**(11), pp. 3826–3834.

[117] Di Schino, A., and Kenny, J. M., 2002, "Effects of the Grain Size on the Corrosion Behavior of Refined AISI 304 Austenitic Stainless Steels," J. Mater. Sci. Lett., **21**(20), pp. 1631–1634.

[118] Helmholtz, H., 1879, "Studien Über Electrische Grenzschichten," Ann. Phys., **243**(7), pp. 337–382.

[119] Burt, R., Birkett, G., and Zhao, X. S., 2014, "A Review of Molecular Modelling of Electric Double Layer Capacitors," Phys. Chem. Chem. Phys., **16**(14), pp. 6519–6538.

[120] Brown, S. D., Tauler, R., and Walczak, B., 2020, *Comprehensive Chemometrics: Chemical and Biochemical Data Analysis*, Elsevier, Amsterdam, Netherlands.

[121] Huang, D. J., and Li, H., 2021, "A Machine Learning Guided Investigation of Quality Repeatability in Metal Laser Powder Bed Fusion Additive Manufacturing," Mater. Des., **203**, p. 109606.

[122]   Ladewig, A., Schlick, G., Fisser, M., Schulze, V., and Glatzel, U., 2016, "Influence of the Shielding Gas Flow on the Removal of Process By-Products in the Selective Laser Melting Process," Addit. Manuf., **10**, pp. 1–9.

[123]   Ma, L., Wiame, F., Maurice, V., and Marcus, P., 2019, "Origin of Nanoscale Heterogeneity in the Surface Oxide Film Protecting Stainless Steel against Corrosion," Npj Mater. Degrad., **3**(1), pp. 1–9.

[124]   Mraied, H., Wang, W., and Cai, W., 2019, "Influence of Chemical Heterogeneity and Microstructure on the Corrosion Resistance of Biodegradable WE43 Magnesium Alloys," J. Mater. Chem. B, **7**(41), pp. 6399–6411.

[125]   Moshiri, M., Candeo, S., Carmignato, S., Mohanty, S., and Tosello, G., 2019, "Benchmarking of Laser Powder Bed Fusion Machines," J. Manuf. Mater. Process., **3**(4), p. 85.

[126]   Ahmed, A., Majeed, A., Atta, Z., and Jia, G., 2019, "Dimensional Quality and Distortion Analysis of Thin-Walled Alloy Parts of AlSi10Mg Manufactured by Selective Laser Melting," J. Manuf. Mater. Process., **3**(2), p. 51.

[127]   Meyer, B., 2012, *Accuracy in Additive Manufacturing: A Common Mistake Is to Confuse High Resolution with Accuracy*, Penton Media, Inc.

[128]   Qin, Y., Qi, Q., Scott, P. J., and Jiang, X., 2019, "Status, Comparison, and Future of the Representations of Additive Manufacturing Data," Comput.-Aided Des., **111**, pp. 44–64.

[129]   Energetics Incorporated, 2013, *Measurement Science Roadmap for Metal-Based Additive Manufacturing*, National Institute of Standards and Technology, U.S. Department of Commerce, Maryland.

[130]   Franchitti, S., Borrelli, R., Pirozzi, C., Carrino, L., Polini, W., Sorrentino, L., and Gazzerro, A., 2018, "Investigation on Electron Beam Melting: Dimensional Accuracy and Process Repeatability," Vacuum, **157**, pp. 340–348.

[131]   Kim, D. B., Witherell, P., Lu, Y., and Feng, S., 2017, "Toward a Digital Thread and Data Package for Metals-Additive Manufacturing," Smart Sustain. Manuf. Syst., **1**(1), pp. 75–99.

[132]   Plesser, H. E., 2018, "Reproducibility vs. Replicability: A Brief History of a Confused Terminology," Front. Neuroinformatics, **11**(76), pp. 1–4.

[133]   McArthur, S. L., 2019, "Repeatability, Reproducibility, and Replicability: Tackling the 3R Challenge in Biointerface Science and Engineering," Biointerphases, **14**(2), p. 020201.

[134]   ISO 5725-1, 1994, *Accuracy (Trueness and Precision) of Measurement Methods and Results - Part 1: General Principles and Definitions*, International Organization for Standardization, Geneva, Switzerland.

[135]   National Academies of Sciences, Engineering, and Medicine, 2019, *Reproducibility and Replicability in Science*, The National Academies Press, Washington, DC.

[136]   ASTM International, "Additive Manufacturing Technology Standards" [Online]. Available: https://www.astm.org/Standards/additive-manufacturing-technology-standards.html.

[137]   ISO/ASTM52900, 2015, *Standard Terminology for Additive Manufacturing - General Principles - Terminology*, ASTM International, West Conshohocken, PA.